MODERN PATHOLOGY

ABSTRACTS (1145–1171)

PATHOBIOLOGY AND EMERGING TECHNIQUES

2022

USCAP 111TH ANNUAL MEETING

REAL INTELLIGENCE

MARCH 19–24, 2022 LOS ANGELES, CALIFORNIA

EDUCATION COMMITTEE

ABSTRACT REVIEW BOARD

1145 Cellular Material from Core Needle Biopsy Washes are Molecularly Representative of the Corresponding Parent Tissue that is Formalin Fixed and Paraffin Embedded

Ayesha Arshad[1], Donald Yergeau[2], Jonathan Bard[3], Wilfrido Mojica[2]
[1]VAWNY, Buffalo, NY, [2]University at Buffalo, SUNY, Buffalo, NY, [3]SUNY Buffalo, Buffalo, NY

Disclosures: Ayesha Arshad: None; Donald Yergeau: None; Jonathan Bard: None; Wilfrido Mojica: None

Background: Cells dislodged during the core needle biopsy (CNB) procedure are an underutilized resource for molecular testing. Previous studies have shown that these cells, if captured and processed to extract their DNA, possess both qualitative and quantitative nucleic acid metrics suitable for high throughput studies. These studies however, have not compared the genetic aberrations between the dislodged cells and their parent tissue and so have not established whether the former can function as a suitable representative of the latter. This study sought to resolve that question by comparing, via next generation sequencing, the mutational profiles between the dislodged, recovered cells and their matched parent, formalin fixed paraffin embedded (FFPE) tissue.

Design: CNB's were performed on five different types of tumors from resection specimens received fresh in the pathology lab. After a brief incubation in buffer, dislodged cells were separated from their parent tissue using a novel sieve based disposable tool. DNA was then separately extracted from the cells and the matched tissue that had undergone FFPE. After generating libraries, the DNA was then sequenced and the data comparatively analyzed.

Results: Qualitatively, the DNA from the dislodged, washed cells had a slightly better overall reference coverage despite similar depth of sequencing than the corresponding parent tissue that underwent FFPE (93.25% vs. 92.75%), and a slightly longer median fragment insert size (107 bp vs 99 bp). Comparison of variant calls per sample at select oncogenic genes indicate high congruence (>85%) between the matched samples in all 5 tumor cases, with discrepancies existing due to filtration of low coverage regions resulting from sequencing depth. Manual inspection of select genes indicate >95% congruence of variants detected between matched samples.

Conclusions: Recovery of dislodged cells from a CNB procedure represents an untapped resource for molecular testing. Herein we have demonstrated that recovered cells that have become dislodged during the CNB procedure and recovered are reflective of the parent tissue at the sequencing level. This finding addresses the following problematic areas: the need to open up more opportunities for molecular testing from these often tissue limited specimens, allowance for more material be used for morphology-based studies (e.g., special stains and immunohistochemistry), and the ability to assure that enough tissue is retained for archival regulatory concerns.

1146 Pathologist Selection of Regions of Interest for Digital Spatial Profiling Demonstrates Association of Tumor Architecture with Pathologic Response to Neoadjuvant Chemo-Immunotherapy in Muscle-Invasive Bladder Cancer

Wolfgang Beck[1], Shilpa Gupta[2], Petros Grivas[3], William Kim[1], Matthew Milowsky[1], Sara Wobker[1]
[1]The University of North Carolina at Chapel Hill, Chapel Hill, NC, [2]Cleveland Clinic, Cleveland, OH, [3]University of Washington, Seattle, WA

Disclosures: Wolfgang Beck: None; Shilpa Gupta: None; Petros Grivas: None; William Kim: None; Matthew Milowsky: None; Sara Wobker: None

Background: Neoadjuvant cisplatin-based chemotherapy is standard of care in muscle-invasive bladder cancer (MIBC) with pathologic response (<ypt2n0) associated="" improved="" survival="" with="">TM Nanostring) can detect and quantify proteins and RNA at highly multiplexed levels. Pathologist selection of regions of interest (ROI) for DSP provides information on tumor architecture, including tumor-enriched, immune-enriched and mixed tumor-immune. We evaluated the association of tumor architecture with response to neoadjuvant chemotherapy-ICI in a cohort of responder (<ypt2) and="" non-responder=""></ypt2)></ypt2n0)>

Design: For each of 36 pre-treatment transurethral resection of bladder tumors (18 < pT2 and 18 ≥pT2), ROIs were selected from H&E stained sections to include 12 independent, randomly sampled ROIs (4 each of tumor-enriched, immune-enriched and mixed tumor-immune) for analysis. Following pathologist selection of ROIs, the H&E selections were aligned with immunofluorescence staining (PanCK and CD45) (Figure 1). Masking was performed to select the tumor-predominant component of interface regions (interface-panCK) and immune-predominant component (interface-CD45). DSP was performed using the NanoString platform with

biomarker panels including immune cell profiling, immunotherapy drug target, immune activation status, immune cell typing, and pan-tumor (total=61 markers for each ROI).

Results: Overall, more DSP biomarkers had significant associations with response when incorporating ROI versus no ROI. Specific biomarkers were further analyzed for their association with therapy response either without incorporating ROIs (All ROIs), or including all ROIs, immune, tumor, interface-CD45 and interface-panCK (Table 1). An association with therapeutic response was seen specific biomarkers, including PD-L1, Ki-67, HLA-DR, HER2, and SMA/FAP-alpha (stroma) when analyzed in the selected ROIs. Using elastic net regression, a model incorporating ROI demonstrated a better fit in biomarker association with response to neoadjuvant chemotherapy-ICI.

Marker	All ROIs	Tumor	Immune	Interface_panCK	Interface_CD45
PD-L1	↑0.024	NS	↑0.068*	NS	NS
Ki-67	↑0.001	↑0.013	↑0.0096	↑0.016	NS
HLA-DR	NS	NS	↑0.029	NS	NS
Her2	NS	↑0.047	NS	NS	NS
SMA+FAP-alpha	↓0.0081	NS	NS	↓0.055*	NS

Table 1: Association of individual DSP markers with response to neoadjuvant chemotherapy-ICI

↑Significant positive association with response (p-value)

↓Significant negative association with response (p-value)

NS = no significant association with response

* trend toward significance

Figure 1 - 1146

Tumor-enriched PanCK — Immune-enriched CD45 — Tumor-Immune Interface PanCK/CD45 — Tumor-Immune Interface Masking — CD45 AOI — PanCK AOI — 001
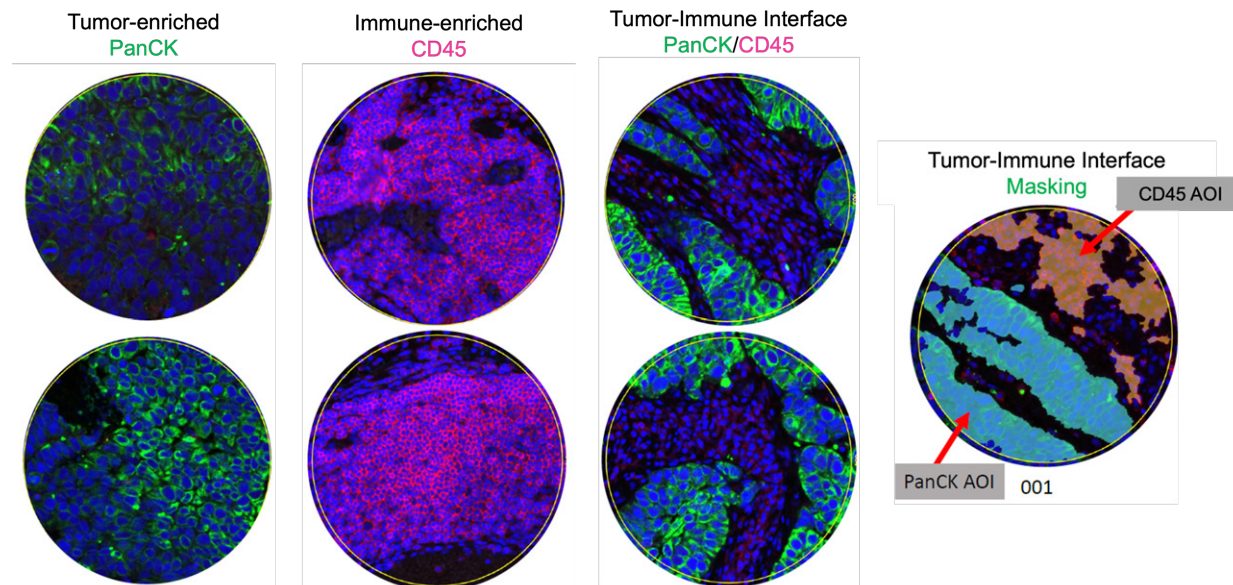
Conclusions: A demonstrated increase in DSP biomarkers in patients with MIBC treated with neoadjuvant chemotherapy-ICI and the association of chemotherapy-ICI pathologic response with specific biomarkers within specific histologically selected ROIs supports further exploration of tumor architecture regarding response and outcomes to neoadjuvant chemo-ICI in MIBC.

1147   Bleach & Stain 15 Marker Multiplex Fluorescence Immunohistochemistry Revealed Six Major PD-L1 Immune Phenotypes with Distinct Spatial Orchestration

Niclas Blessin[1], Elena Bady[1], Tim Mandelkow[1], Cheng Yang[1], Jonas Raedler[1], Ronald Simon[1], Christoph Fraune[1], Maximilian Lennartz[1], Sarah Minner[1], Eike-Christian Burandt[1], Doris Höflmayer[1], Guido Sauter[1], Katharina Moeller[2], Soeren Weidemann[3]

[1]University Medical Center Hamburg-Eppendorf, Hamburg, Germany, [2]Universitaetsklinikum Hamburg-Eppendorf, Hamburg, Germany, [3]University Hospital Hamburg, Hamburg, Germany

Background: Highly multiplexed fluorescence immunohistochemistry (IHC) enables quantification of immune checkpoints such as PD-L1 (programmed cell death ligand 1), PD-1 (programmed cell death protein 1) or CTLA-4 (cytotoxic T-lymphocyte-associated protein 4) in the tumor microenvironment (TME). However, a framework to assess the spatial orchestration of these markers and immune cells has yet to be established.

Design: To study the impact of PD-L1, PD-1 and CTLA-4 expression on the TME and patient's outcome, a framework for automated immune checkpoint quantification on tumor and immune cells was established and validated. Automated immune checkpoint quantification was facilitated by incorporating three different deep learning steps for the analysis of 44 different human carcinomas from 3098 tumor specimens using a bleach & stain 15-marker multiplex fluorescence IHC panel was used for this study (i.e., PD-L1, PD-1, CTLA-4, panCK, CD68, CD163, CD11c, iNOS, CD3, CD8, CD4, FOXP3, CD20, Ki67, CD31).

Results: Comparing the automated deep-learning based PD-L1 quantification with brightfield PD-L1 data revealed a high concordance in tumor and immune cells ($p<0.0001$ each). Incorporating the spatial orchestration and immune checkpoint expression of T-cell subsets, dendritic cells (DC) and macrophage subsets enables the identification of 6 major phenotypes – according to the degree of inflammation – within the cases showing PD-L1 expression on tumor cells (G1), exclusively on immune cells (G2), and a lack of PD-L1 expression (G3). A high intratumoral macrophage density, a high degree of T-cell exclusion, a high PD-1 expression on T-cells, and a low CTLA-4 expression level on T-cells was significantly associated with the inflamed PD-L1 immune phenotype ($p<0.001$ each). Although a high M1 macrophage (CD68+iNOS+CD163-) density was linked to the non-inflamed PD-L1$^+$ macrophage phenotype ($p=0.048$), all other macrophage and DC subsets (identified by CD68, CD163, CD11c, iNOS) as well as T-cell subsets (identified by CD3, CD8, CD4, FOXP3) were a hallmark to the inflamed PD-L1 immune phenotypes ($p<0.001$ each). In breast cancer, the PD-L1 intensity on tumor cells showed a higher predictive performance for overall survival with an area under receiver operating curves (AUC) of 0.72 ($p<0.0001$) than the percentage of PD-L1$^+$ tumor cells (AUC: 0.54).

Conclusions: In conclusion, a highly multiplexed fluorescence IHC framework for automated PD-L1, PD-1 and CTLA-4 assessment revealed that PD-L1 positive tumor samples can be also associated with a non-inflamed TME and high spatial T-cell exclusion.

1148   One Man's Trash... A Demonstration of the Utility of Heritage Specific Single Nucleotide Polymorphisms (SNPs) in a Clinical Setting

Matthew Carda[1], Daniel Harter[1], Jesse Cox[1]
[1]University of Nebraska Medical Center, Omaha, NE

Background: Analysis of next-generation sequencing (NGS) data takes several factors into consideration when assessing the significance of identified variants. To this, population studies of germline polymorphisms (SNPs) can help distinguish potentially significant changes from those that would be expected within a given population.

Design: We hypothesize that identification of this class of SNPs, while traditionally only used in forensics and genealogy applications, can be utilized for clinical purposes to monitor disease state and post-transplantation status. Herein, we describe a case of an individual of African descent who had developed treatment associated myelodysplastic syndrome (MDS—refractory anemia with excess blasts) following treatment of diffuse large B-cell lymphoma.

Results: During the diagnostic workup of his MDS, a pathogenic NRAS mutation (p.G13D, VAF: 14.5%) was identified, as well as two additional variants suspected to be germline SNPs (TET2 p.S145N, VAF: 49.1% and ASXL1 p.K838R, VAF: 51.5%). The TET2 and ASXL1 variants, while found only at 0.07% and 0.3% within a general population, respectively, are each enriched 10-fold in persons with African heritage. The patient underwent bone marrow ablation and transplant to treat his MDS. On follow-up NGS testing, three novel variants were identified suspected of belonging to the patient's unrelated donor as well as one variant shared between donor and recipient [Figure 1], whom appeared to also be of African descent. This suspicion would be consistent with the observation that the recipient's Human-Leukocyte Antigen (HLA) type was enriched for alleles common in African populations [Figure 2]. We further identified low level residual TET2 p.S145N in the follow-up NGS sample (VAF: ~2.0%), likely to be derived from residual recipient hematopoietic elements.

Figure 1 - 1148

Figure 2 - 1148
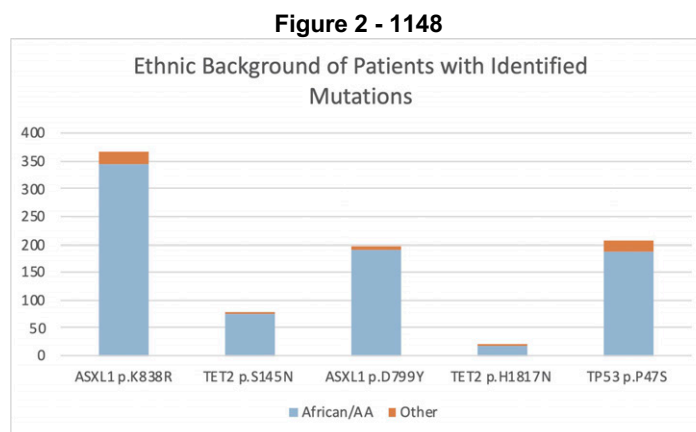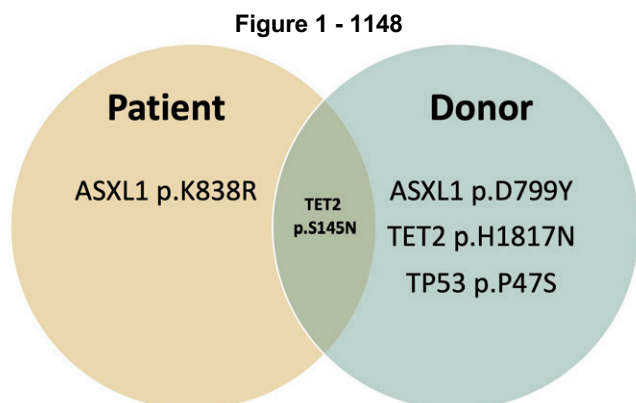
Conclusions: Overall, this case demonstrates the interconnections of multiple disciplines within pathology. Moreover, it emphasizes the clinical utility of identifying and tracking SNPs unique to an individual and common within various ethnic groups. We believe this highlights a potentially novel clinical utility in the standard approach to reviewing NGS data, which would otherwise be disregarded. Alongside concurrent standards of care, evaluation and monitoring of unique SNPs has the potential to provide valuable and cost-effective data. This could further enhance the ability to monitor engraftment status and elevate the quality of patient care in a vulnerable population.

1149 Trophoblast Cell Surface Antigen 2 (TROP2) Expression in Human Tumors: A Tissue Microarray Study on 18,563 Tumors

David Dum[1], Anne Menz[1], Doris Höflmayer[1], Maximilian Lennartz[1], Christoph Fraune[1], Christian Bernreuther[2], Guido Sauter[1], Ria Uhlig[1], Waldemar Wilczak[1], Stefan Steurer[3], Sarah Minner[1], Ronald Simon[1], Eike-Christian Burandt[1], Till Krech[1]
[1]University Medical Center Hamburg-Eppendorf, Hamburg, Germany, [2]University Medical Center Hamburg-Eppendorf, [3]University Medical Center Hamburg-Eppendorf, Germany

Background: Trophoblast cell surface antigen 2 (TROP2) is the target of sacituzumab govitecan (SG), an antibody-drug conjugate that was recently approved for previously treated triple negative breast cancer and urothelial carcinomas.

Design: To comprehensively determine TROP2 expression in normal and neoplastic tissues, a tissue microarray containing 18,563 samples from 150 different tumor types and subtypes as well as 608 samples of 76 different normal tissue types was analyzed by immunohistochemistry.

Results: TROP2 positivity was found in most normal epithelial cell types and in 109 of 150 tumor categories, including 92 of 95 epithelial tumor categories. 82 epithelial tumor entities had at least one case showing strong TROP2 positivity. Particularly high rates of positivity and highest expression levels were seen in squamous cell carcinomas of various origins and various categories

of urothelial, breast, prostate, pancreatic, and ovarian cancers (>95% positive). High TROP2 expression was linked to advanced stage (p=0.0069) and nodal metastasis (p<0.0001) in colorectal cancer as well as to nodal metastasis in gastric adenocarcinoma (p=0.0246) and papillary thyroid cancer (p=0.0013). Low TROP2 expression was linked to advanced stage in urothelial carcinoma (p<0.0001), high pT (p=0.0024) and high grade (p<0.0001) in breast cancer, as well as with high grade (p=0.0005) and pT stage (p=0.0009) in papillary renal cell carcinomas. Associations between TROP2 expression and clinicopathological features were not found in clear cell renal cell carcinomas, high grade serous ovarian carcinomas, pancreatic adenocarcinomas and in endometroid endometrium carcinomas.

Conclusions: In summary, TROP2 is abundantly expressed in a broad range of epithelial neoplasms. Both TROP2 upregulation and downregulation can be associated with cancer progression in a tumor type dependent manner. As anti-TROP2 cancer drugs have demonstrated efficiency and induce tolerable side effects they may be applicable to a broad range of tumor entities in the future.

1150 Comparisons of Screening Strategies for Lynch Syndrome among Patients with Colorectal Cancer

Xu Feng[1], Qianming Bai[2], Xiaoyan Zhou[3]
[1]*Fudan University Shanghai Cancer Center, Fudan University, Shanghai, China,* [2]*Fudan University Shanghai Cancer Center, Shanghai, China,* [3]*Fudan University Shanghai Cancer Center, Shanghai Medical College, Fudan University, Shanghai, China*

Disclosures: Xu Feng: None; Qianming Bai: None; Xiaoyan Zhou: None

Background: Lynch syndrome (LS) is the most common hereditary colorectal cancer, which caused by germline pathogenic mutations in one of four mismatch repair genes or EPCAM deletion. Guidelines or consensus are available on LS screening, however, with the refinement of essential biomarkers in diagnosis and treatment of CRC, next-generation sequencing (NGS) is increasingly being applied in clinical practice. Our study intends to evaluate the advantages and limitations of tumor sequencing for LS screening and compare it with the classic strategy so as to provide better recommendations for clinical practice.

Design: Between June 2017 and March 2021, 585 cases with colorectal cancer were selected. All cases were tested by IHC and NGS. The DNA methylation status of MLH1 promoter and p.V600E status of BRAF in MLH1-deficient cases were detected. Germline mutation testing was performed among cases with tumor MMR or EPCAM pathogenic or likely pathogenic mutations. The germline large genomic rearrangements (LGRs) was detected among dMMR or MSI-H cases with MMR or EPCAM germline mutation (SNV/indel) negative.

Results: Among 585 cases , 26.8% (157) demonstrated MSI-H and 73.2% (428) demonstrated MSS or MSI-L by NGS, 28% (164) demonstrated dMMR and 72% (421) demonstrated pMMR by IHC, the concordance rate between NGS and IHC was 98.1% (574/585). Among cases with MLH1-deficient, 39.2% (42/107) were MLH1-methylated and 12.1% (13/107) were BRAF p.V600E mutated. Tumor sequencing showed that 75.7% (125/165) patients carried at least one pathogenic or likely pathogenic MMR genes mutation in MSI-H or dMMR cases and 1.4% (6/420) in MSS/pMMR cases. Germline single site testing identified 62 LS cases and three of them were MLH1-methylated. Germline LGRs testing identified 3 MLH1-deletion, 6 MSH2-deletion and 3 PMS2-deletion. Although the majority of patients with LS exhibited MSI-H or dMMR, one patient showed MSS and pMMR, another two showed MSS but dMMR. The distribution of MMR germline mutation in those LS cases was as follows: MLH1, 41.9% (31/74); MSH2, 41.9% (31/74); MSH6, 9.4% (7/74); PMS2, 6.8% (5/74).

Conclusions: LS was not only identified in MLH1-unmethylated cases, but also in MLH1-methylated or MSS cases, which suggested that LS screening strategy based on MMR protein would have the risk of missing LS patients. Apart from detecting variants in MMR genes, tumor sequencing was also optimized to detect for other cancer susceptibility genes and simplify the workflow of LS screening.

1151 Artificial Intelligence-Powered Analyzer Reduces Inter-observer Variation in PD-L1 Tumor Proportion Score of Non-Small Cell Lung Cancer

Seokhwi Kim[1], Sangjoon Choi[2], Soo Ick Cho[3], Hyojin Kim[4], Minuk Ma[5], Sergio Pereira[6], Seonwook Park[6], Brian Aum[6], Seunghwan Shin[6], Kyunghyun Paeng[6], Donggeun Yoo[6], Wonkyung Jung[5], Chan-Young Ock[6], Se-Hoon Lee[7], Jin-Haeng Chung[8], Yuna Choi[9]

[1]Ajou University School of Medicine, Suwon, South Korea, [2]Samsung Medical Center, Seoul, South Korea, [3]Lunit Inc., Gang nam gu, South Korea, [4]Seoul National University Bundang Hospital, Seongnam, South Korea, [5]Lunit Inc., Gangnamgu, South Korea, [6]Lunit Inc., Seoul, South Korea, [7]Samsung Medical Center, Sungkyunkwan University School of Medicine, Seoul, South Korea, [8]Seoul National University Bundang Hospital, Seoul, South Korea, [9]Samsung Medical Center, South Korea

Background: Programmed death ligand 1 (PD-L1) expression level is a prognostic marker in predicting response to immune checkpoint inhibitors (ICIs) in advanced non-small cell lung cancer (NSCLC). However, manual evaluation of the PD-L1 tumor proportion score (TPS) often leads to inter-observer variation. Whether artificial intelligence (AI) assistance could improve the accurate TPS reading and hence lead to better prediction of the ICI response have not been studied yet.

Design: An AI-powered analyzer, LUNIT SCOPE PD-L1 TPS was developed with a total of 393,565 tumor cells from 802 whole-slide images (WSIs) of NSCLC, annotated by board-certified pathologists. Three independent pathologists scored PD-L1 TPS in an external cohort of 479 patients. They then had chances to revise the initial TPS groups (<1%, 1%–49%, and ≥50%) with AI assistance. They independently reviewed cases that the TPS group had been changed after AI model assistance despite the initial concordance among them (human misinterpretation) and cases that the group had not been changed despite the AI suggestion of other TPS groups (AI misinterpretation). The effect on clinical outcome of AI-assisted revised TPS group was also analyzed in 430 patients treated with second or later ICIs.

Results: Initially, the three pathologists concordantly scored TPS in 81.4% of cases. Following the revision of their score by adopting AI's suggestion of TPS group other than their baseline value (N = 91, 93, and 107 for each pathologist), the overall concordance rate was increased to 90.2% (P < 0.001). The potential human misinterpretation cases include simple under-/overestimation (74.2%), difficulty due to artifacts (12.9%), and difficulty due to cellular morphology (12.9%) (Figure 1). The potential AI misinterpretation cases include false-negative readings of PD-L1-negative normal epithelium (66.7%), false-negative readings of PD-L1-positive tumor cell (19.0%), and false-positive readings of PD-L1-positive macrophage (14.3%). The revised TPS group with AI assistance predicted objective response rate, progression-free survival, and overall survival better than the baseline group without AI assistance (Figure 2).

Figure 1 - 1151

Figure 2 - 1151

A

	TPS (%)	N	ORR (%, n)	Median PFS (months, 95% CI)	HR (95% CI)	P-value	Median OS (months, 95% CI)	HR (95% CI)	P-value
Baseline	< 1	74	6.8 (5)	1.9 (1.4-2.8)	Ref.	Ref.	8.3 (6.6-14.4)	Ref.	Ref.
	1–49	150	17.3 (26)	2.4 (1.9-3.5)	0.73 (0.55-0.99)	0.040	13.7 (8.3-24.4)	0.77 (0.51-1.13)	0.2
	≥ 50	206	31.1 (64)	3.5 (2.3-4.8)	0.60 (0.45-0.79)	<0.001	16.2 (14.0-NA)	0.67 (0.47-0.97)	0.035

Baseline TPS (without AI)

B

	TPS (%)	N	ORR (%, n)	Median PFS (months, 95% CI)	HR (95% CI)	P-value	Median OS (months, 95% CI)	HR (95% CI)	P-value
Revised	< 1	53	5.7 (3)	1.8 (1.4-2.9)	Ref.	Ref.	7.7 (5.3-13.8)	Ref.	Ref.
	1–49	174	13.2 (23)	2.2 (1.8-2.8)	0.77 (0.56-1.06)	0.11	13.7 (8.2-19.3)	0.69 (0.46-1.04)	0.073
	≥ 50	203	34.0 (69)	3.8 (2.8-6.4)	0.52 (0.38-0.72)	<0.001	16.8 (14.2-NA)	0.56 (0.37-0.84)	0.005

Revised TPS (with AI assistance)
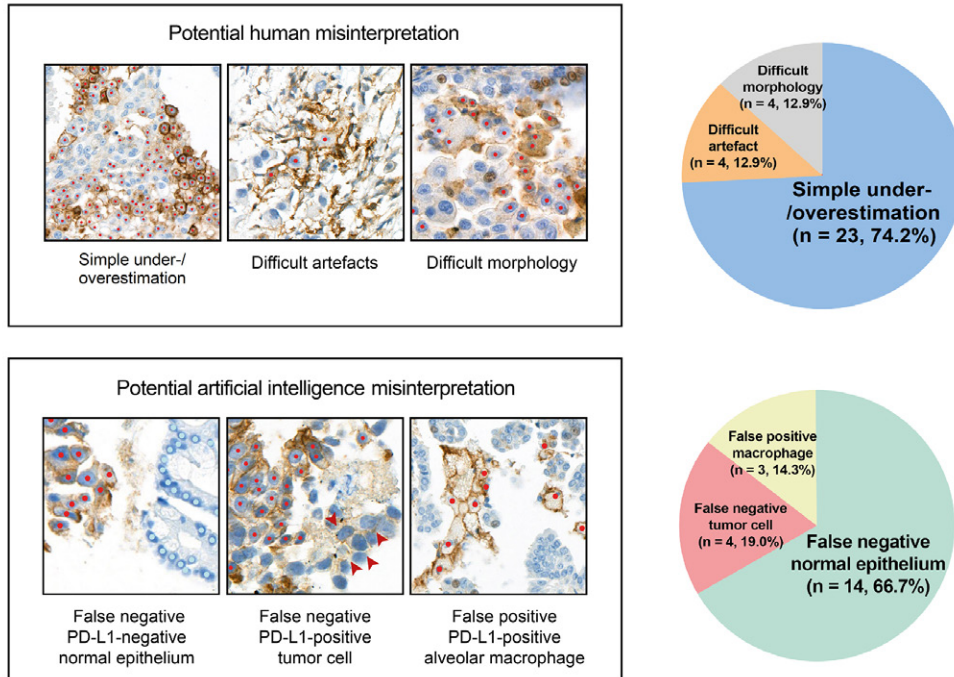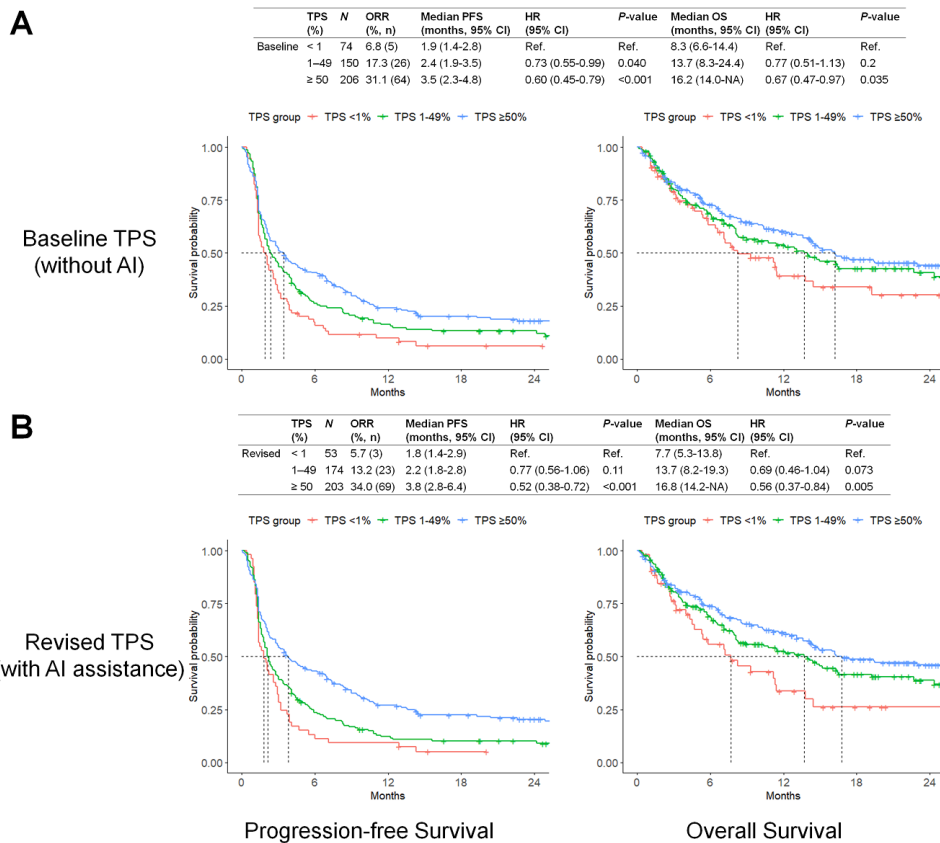

Progression-free Survival   Overall Survival

Conclusions: Assistance with the AI-powered TPS analyzer improved the pathologists' consensus and prediction of the clinical response. In utilizing AI models, pathologists could interpret PD-L1 expression more accurately by understanding the weaknesses of pathologists and AI models.

1152 Development and Validation of the Confocal Laser Endomicroscopic System for the Real-Time Histologic Evaluation of Gastric Cancer Surgical Specimens

Seokhwi Kim[1], Hyunsik Bae[2], Jinah Chu[3], Haeyon Cho[4], Sangjoon Choi[5], Kyungmin Hwang[6], Yeonju Jo[6]
[1]Ajou University School of Medicine, Suwon, South Korea, [2]Armed Forces Hospital, Seongnam, South Korea, [3]Kangbuk Samsung Hospital, Sungkyunkwan University School of Medicine, South Korea, [4]Asan Medical Center, University of Ulsan College of Medicine, Seoul, South Korea, [5]Samsung Medical Center, Seoul, South Korea, [6]VPIX Medical Inc, Daejeon, South Korea

Disclosures: Seokhwi Kim: None; Hyunsik Bae: None; Jinah Chu: None; Haeyon Cho: None; Sangjoon Choi: None; Kyungmin Hwang: None; Yeonju Jo: None

Background: Despite the need for instant histological evaluation of a fresh tissue, available method is limited to the conventional frozen section technique which has drawbacks including processing time and preparation artifacts. A newly developed digital-based confocal laser endomicroscopic system can provide a real-time imaging of tissue without producing slides. We here evaluated its applicability in surgical specimen.

Design: A confocal laser endomicroscopic system using 488 nm light source (cCeLL-A 488) was developed for slide-free imaging of tissues (Figure 1). Twenty-seven gastric advanced cancer tissues and the same number of normal gastric tissues were obtained from nine patients. Following the fluorescein sodium staining of the tissue, a miniaturized microscope head directly contacted and irradiated the tissue with a Lissajous pattern laser scanning to acquire images. The tissue was lively visualized with a 500x500um field of view. Two-hundred images from mucosa, submucosa, proper muscle and subserosa were obtained. Five board-certificated pathologists reviewed 100 endomicroscopic images and detect histologic locations and the presence of cancer cells. The matched hematoxylin and eosin (H&E) staining of the tissues, acquired after the fixation, were given for the comparison (Figure 2). The pathologists' performances for the interpretation were again evaluated with additional 100 endomicroscopic images.

Results: Initially, the pathologists could identify the histologic location of the endomicroscopic images with average 65.7% accuracy and distinguish cancer tissue from normal with average 74.7% accuracy. The average sensitivity and specificity of cancer tissue detection were 71.9% and 76.1% and the average reading time per image was 12.0 seconds. After the training with matched H&E images, the pathologists showed significantly improved performance. They identified the histologic location with average 92.8% accuracy and detect cancer tissue with average 90.9% accuracy. The average sensitivity and specificity of cancer tissue detection were increased to 89.1% and 93.2% and the average reading time per image was decreased to 5.3 seconds.

Figure 1 - 1152

Figure 2 - 1152

Normal — Adenocarcinoma moderately differenetiated — Poorly cohesive carcinoma
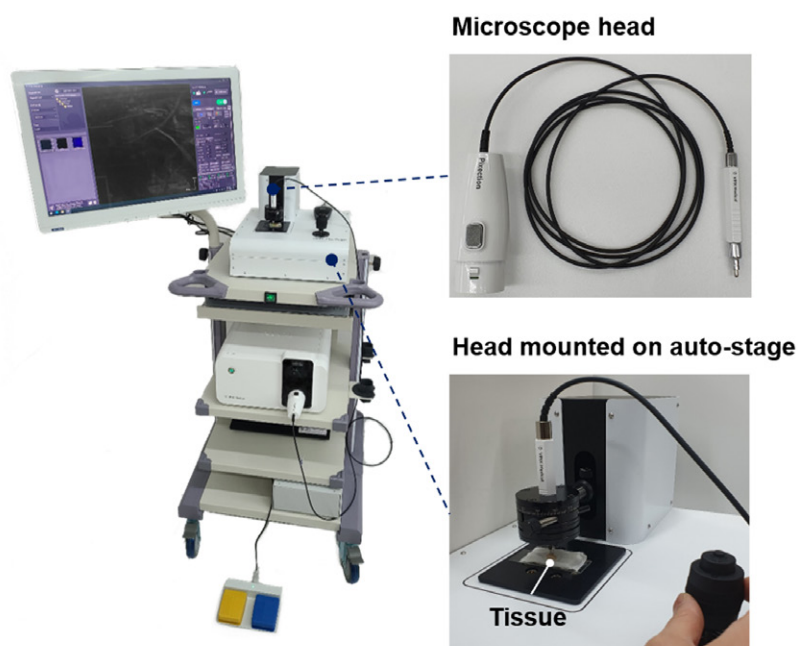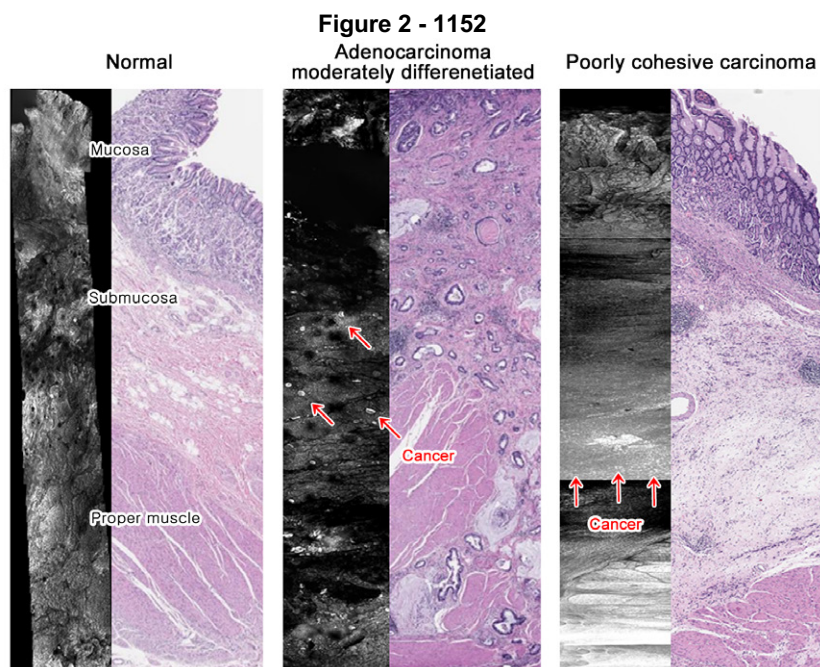
Conclusions: The confocal laser endomicroscopic system enabled the immediate acquisition of high-quality histomorphologic images. The accurate analysis of the cancer cells and histologic location was possible with operator training which raises its potential value as an alternative or assistant modality for real-time tissue imaging.

1153 PD-L1/PD-1 Proximity Assay: Witnessing the Real Protein-Protein Interaction

Faruk Erdem Kombak[1], Umesh Bhanot[1], Asako Tanaka[1], Kateryna Ondrejkovic[1], Irina Linkov[1], Marina Asher[1], Adrian Murillo[2], Joachim Silber[1], Michael Roehrl[1]
[1]Memorial Sloan Kettering Cancer Center, New York, NY, [2]Ventana Medical Systems, Inc., Oro Valley, AZ

Background: Current evaluation methods for PD-L1 do not provide information about engagement with its PD-1 receptor. Demonstrating the protein-protein interaction between PD-L1 and PD-1 could be a better predictor of response to immune checkpoint inhibitor treatment.

Design: For this study, a total of 32 cases were recruited retrospectively. Diagnoses included 7 pulmonary adenocarcinomas, 5 malignant melanomas, 9 gastric adenocarcinomas, 4 squamous cell carcinomas (head & neck), 3 colonic adenocarcinomas, 2 urothelial carcinomas, 1 invasive ductal carcinoma of the breast, and 1 high-grade serous carcinoma of the ovary. All cases underwent single PD-L1 (SP263) and PD-1 (NAT105) immunohistochemistry (IHC) before Proximity assay (PA).

The Proximity Assay utilizes a caged anti-rabbit DIG secondary antibody which is uncaged by the alkaline phosphatase of the anti-mouse AP conjugate, but only if the two are in close spatial proximity (<40 nm), indicating direct PD-1/PD-L1 binding. DIG, if uncaged, is detected by anti-DIG POD and visualized with DAB.

PD-L1 positivity was quantified as a combined positivity score (CPS) and PD-L1 as a percentage of positive immune cells. Proximity signals were classified as negative/rare/prominent based on distribution and density.

Results: All cases with both PD-L1 and PD-1 expression showed intercellular and granular staining on PA. PD-L1+/PD-1-, PD-L1-/PD-1+, and PD-L1-/PD-1- cases by individual IHC were all negative in PA, as expected. Positive PA cases showed scattered staining in general (Figure 1), except 2 cases with 45% PD-L1+ & 70% PD-1+ and 20% PD-L1+ & 30% PD-1+ showed prominent PA staining (Figure 2).

Figure 1 - 1153
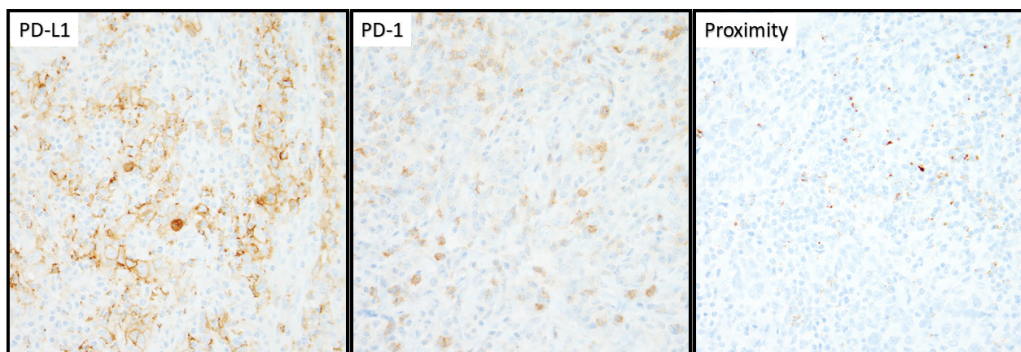
Figure 2 - 1153
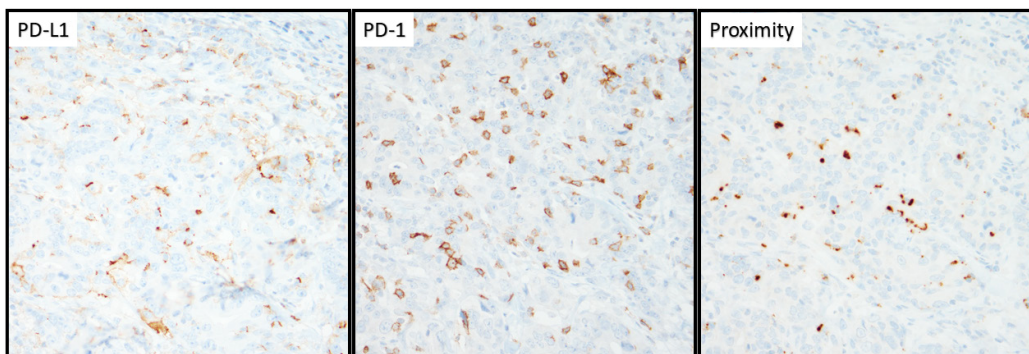
Conclusions: Our preliminary results show that the novel PD-1/PD-L1 Proximity Assay staining is sensitive and specific for detecting the direct physical interaction between PD-L1 and PD-1 expressing cells. The degree of PA staining is dependent on immune cell distribution, rather than the individual absolute levels of PD-L1/PD-1 expression. We believe these striking findings about PD-1/PD-L1 engagement may provide a powerful companion diagnostic for immunotherapy.

1154 Simultaneous Bright Field Chromogenic Multiplex Immunohistochemistry with HRP-Based New Chromogens: A Better and More Precise Way of PD-L1 Scoring with Added Benefits

Faruk Erdem Kombak[1], Umesh Bhanot[1], Asako Tanaka[1], Kateryna Ondrejkovic[1], Irina Linkov[1], Marina Asher[1], Adrian Murillo[2], Joachim Silber[1], Michael Roehrl[1]
[1]Memorial Sloan Kettering Cancer Center, New York, NY, [2]Ventana Medical Systems, Inc., Oro Valley, AZ

Disclosures: Faruk Erdem Kombak: None; Umesh Bhanot: None; Asako Tanaka: None; Kateryna Ondrejkovic: None; Irina Linkov: None; Marina Asher: None; Adrian Murillo: None; Joachim Silber: None; Michael Roehrl: None

Background: Evaluation of PD-L1, the current focus of immune checkpoint inhibitor therapies, has been a problematic task for pathologists. The need for discriminative scoring requires better techniques. Our simultaneous bright field chromogenic multiplex immunohistochemistry approach enhanced with HRP-based chromogens and organ/origin-defining markers can be a promising solution.

Design: For multiplex (triple) IHC design, a total of 44 cases were used. Yellow chromogen was selected for nuclear labeling, paired with different antibodies interchangeably targeting the tissue origin or the type of the tumor sample used (Table 1). Red chromogen was matched with PD-L1 and blue was matched with Cytokeratin or HMB45 for secondary cytoplasmic labeling. Red, yellow, and blue HRP detections utilize a tyramide-based, two-step, HRP-mediated process which results in the chromogen covalently depositing on the tissue. All three HRP-based chromogens were used in combination with each antibody, along with DAB singleplex for comparison.

Results: All triplex designs exhibited selective, easily distinguishable, and strong immunoreactivity (Figure 1 (SCC), Figure 2 (melanoma)). Non-specific background staining was minimal both in single and triplex runs. In comparison, triplex design showed singleplex-equivalent performance for Combined Positive Scoring of PD-L1 (R^2=0.9919), yet also provides simultaneous unequivocal distinction between cell type and cancer type on the same slide.

Table 1. Chromogen-antibody pairs and types of tumors used in multiplex designs

	Yellow	Red	Blue	Tumor types
Design 1	TTF-1 (NCL-L-TTF1)	PD-L1 (SP263)	Cytokeratin (AE1&AE3)	Pulmonary adenocarcinoma
Design 2	CDX2 (EPR2764Y)	PD-L1 (SP263)	Cytokeratin (AE1&AE3)	Colorectal adenocarcinoma
Design 3	GATA3 (L50-823)	PD-L1 (SP263)	Cytokeratin (AE1&AE3)	Breast and bladder carcinomas
Design 4	p40 (BC-28)	PD-L1 (SP263)	Cytokeratin (AE1&AE3)	Squamous cell carcinoma
Design 5	PAX8 (10336-1-AP)	PD-L1 (SP263)	Cytokeratin (AE1&AE3)	Renal cell and ovarian carcinomas
Design 6	SOX10 (BC34)	PD-L1 (SP263)	HMB45 (HMB-45)	Malignant melanoma

Figure 1 - 1154
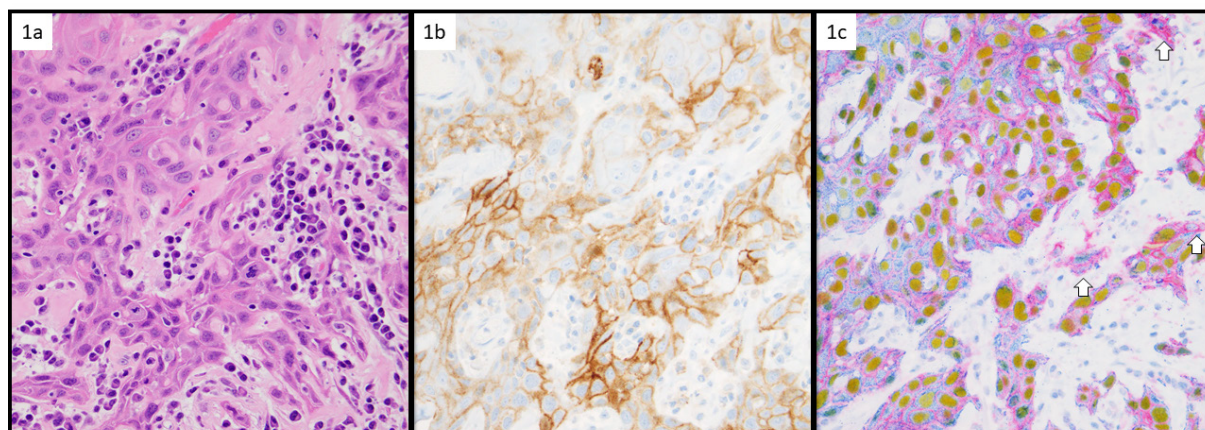
Figure 2 - 1154
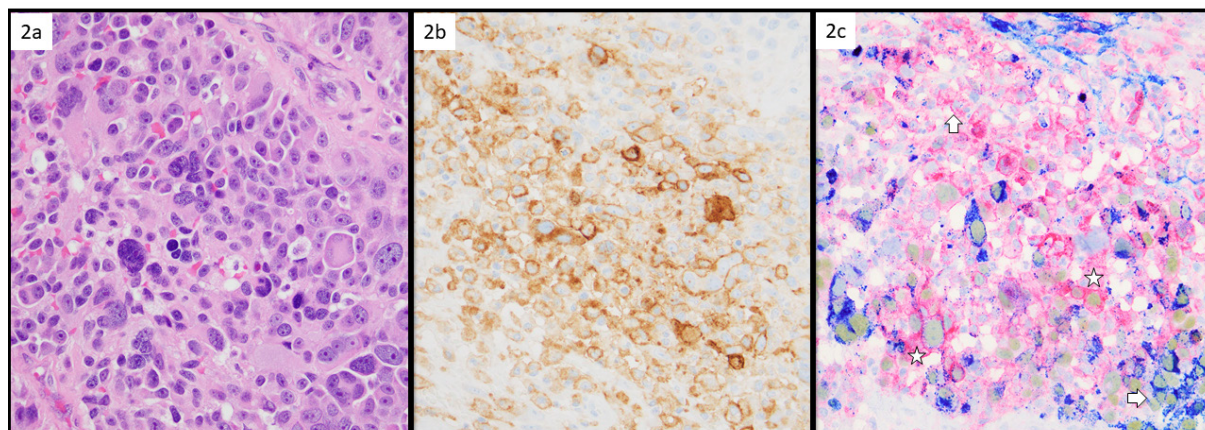
Conclusions: Our multiplex designs with PD-L1 and organ/cell type-defining markers is a novel technique to precisely evaluate PD-L1 expression on tumor cells and inflammatory cells separately on the same section. Integration of these auxiliary markers with PD-L1 also assists in differential diagnosis, especially in difficult occasions where only a small amount of tissue is available, origin of the metastatic tumor is unknown, or the tumor itself is not known to be primary or metastatic.

1155 Immune Programs Associated to Tumoral Tertiary Lymphoid Structures at Different Maturation Stages in Early-Stage Lung Adenocarcinoma

Rossana Lazcano[1], Pedro Rocha[2], Sharia Hernandez[1], Jay Mehta[3], Anthony Kang[1], Kasthuri Kannan[1], Wei Lu[1], Steven Powell[1], Khaja Khan[1], Edwin Parra[1], Jianling Zhou[1], Renganayaki Pandurengan[1], Jianjun Zhang[1], Tina Cascone[1], Carmen Behrens[1], Cara Haymaker[1], Linghua Wang[1], Ignacio Wistuba[1], Humam Kadara[1], Luisa Solis Soto[1]
[1]The University of Texas MD Anderson Cancer Center, Houston, TX, [2]Hospital del Mar-Parc de Salut Mar, Barcelona, Spain, [3]Rice University, Houston, TX

Disclosures: Rossana Lazcano: None; Pedro Rocha: None; Sharia Hernandez: None; Jay Mehta: None; Anthony Kang: None; Kasthuri Kannan: None; Wei Lu: None; Steven Powell: None; Khaja Khan: None; Edwin Parra: None; Jianling Zhou: None; Renganayaki Pandurengan: None; Jianjun Zhang: None; Tina Cascone: None; Carmen Behrens: None; Cara Haymaker: None; Linghua Wang: None; Ignacio Wistuba: None; Humam Kadara: None; Luisa Solis Soto: None

Background: Tertiary lymphoid structures (TLS) are ectopic lymphoid organs that have being recently associated with better outcomes and response to immune therapy in lung adenocarcinoma. The neogenesis of tumoral TLS and its impact in regulating the tumor microenvironment of lung cancer is still unknown. We aimed to preliminarily immunoprofile TLS to identify high-potential biomarkers that are differentially expressed in intratumoral (IT) TLS compared to TLS in adjacent lung (AL), and at different stages of TLS maturation.

Design: We selected 12 FFPE surgically resected stage I lung adenocarcinoma samples. The samples were immunostained with CD20, CD21 and CD23 to identify and classify B-cell lymphoid clusters in: lymphoid aggregates (LA), immature TLS (iTLS) and mature TLS (mTLS) in IT and AL. Serial sections were used to perform GeoMx Digital Spatial profiling (NanoString) with CD20, CD3 and CK mIF to select Regions of Interest (ROI) and profile 49 immune biomarkers. The ROI selection strategy was: representative TLS, LA and areas with B-cell diffuse immune infiltration were selected and 2 segments were obtained from each ROI based on the expression of CD20 and CD3 (B-cell and T-cell enriched) **(Figure 1)**. Data were normalized using background correction. Statistical analyses were performed using GeoMx DSP analysis tools.

Results: We profiled 263 segments (IT: B-cell TLS/LA, n=64; T-cell TLS/LA, n=70 ;B-cell diffuse, n=18; T-cell diffuse, n= 37; tumor cells, n=36. AL: B-cell TLS/LA, n=19; T-cell TLS/LA, n=19). B-cell segments of IT mTLS had higher protein counts for HLA-DR and CD127 compared to IT iTLS (p<0.05), and higher Granzyme B, HLA-DR and CD45 counts compared to LA (p<0.05). T-cell segments of IT iTLS had higher counts of TIM3 (p<0.05) compared to IT mTLS. B-cell segments of IT mTLS showed higher counts of OX40L, GITR, CD45RO and CD8 compared to AL mTLS (p<0.05). T-cell segments from IT mTLS had higher counts of CD127, OX40L, CD45RO, B7H3 and CD34 compared to AL mTLS (p<0.05). **(Table 1)**

Table 1. Immune biomarkers differentially expressed in TLS B-cell enriched areas and T-cell enriched areas.

Immune markers	Biomarkers differentially expressed at Different IT TLS maturation						Biomarkers differentially expressed by TLS location			
	IT mTLS vs IT iTLS		IT mTLS vs IT LA		IT iTLS vs IT LA		IT mTLS vs AL mTLS		IT iTLS vs AL iTLS	
	B-cell area	T-cell area	B-cell area	T-cell area	B-cell area	T-cell area	B-cell area	T-cell area	B-cell area	T-cell area
HLA-DR	↑ IT mTLS	ns	↑ IT mTLS	ns	ns	ns	ns	ns	ns	↑ IT iTLS
CD127	↑ IT mTLS	ns	ns	ns	ns	ns	ns	↑ IT mTLS	↑ IT iTLS	ns
OX40L	ns	ns	ns	ns	ns	ns	↑ IT mTLS	↑ IT mTLS	↑ IT iTLS	ns
CD45RO	ns	ns	ns	ns	ns	ns	↑ IT mTLS	↑ IT mTLS	↑ IT iTLS	↑ IT iTLS
CD44	ns	ns	ns	ns	ns	ns	ns	ns	↑ IT iTLS	↑ IT iTLS
Granzyme B	ns	ns	↑ IT mTLS	ns	ns	ns	ns	ns	↑ IT iTLS	ns
CD68	ns	ns	ns	ns	ns	ns	ns	ns	↑ IT iTLS	ns
B2-microglobulin	ns	ns	ns	ns	ns	ns	ns	ns	↑ IT iTLS	ns
B7H3	ns	ns	ns	ns	ns	ns	ns	↑ IT mTLS	ns	↑ IT iTLS
GITR	ns	ns	ns	ns	ns	ns	↑ IT mTLS	ns	ns	ns
CD8	ns	ns	ns	ns	ns	ns	↑ IT mTLS	ns	ns	ns
CK	ns	ns	ns	ns	ns	ns	↑ IT mTLS	ns	ns	ns
4-1BB	ns	ns	ns	ns	ns	ns	ns	ns	ns	ns
CTLA4	ns	ns	ns	ns	ns	ns	ns	ns	ns	ns
CD4	ns	ns	ns	ns	ns	ns	ns	ns	ns	↑ IT iTLS
CD25	ns	ns	ns	ns	ns	ns	ns	ns	ns	↑ IT iTLS
Foxp3	ns	ns	ns	ns	ns	ns	ns	ns	ns	ns
CD34	ns	ns	ns	ns	ns	ns	ns	↑ IT mTLS	ns	ns
CD45	ns	ns	↑ IT mTLS	ns	↑ IT iTLS	ns	ns	ns	ns	ns
Fibronectin	ns	ns	ns	↑ IT LA	ns	ns	ns	ns	ns	ns
TIM3	ns	↑ IT iTLS	ns	ns	ns	ns	ns	ns	ns	ns

p value<0.005 was considered statistically significant; ns, nonsignificant; IT, Intratumoral, AL, adjacent lung; mTLS, mature TLS; iTLS, immature TLS; LA, lymphoid aggregate

Figure 1 - 1155

Figure 1. TLS classification and Digital Spatial Profiling (DSP) region of interest (ROI) selection and segmentation.
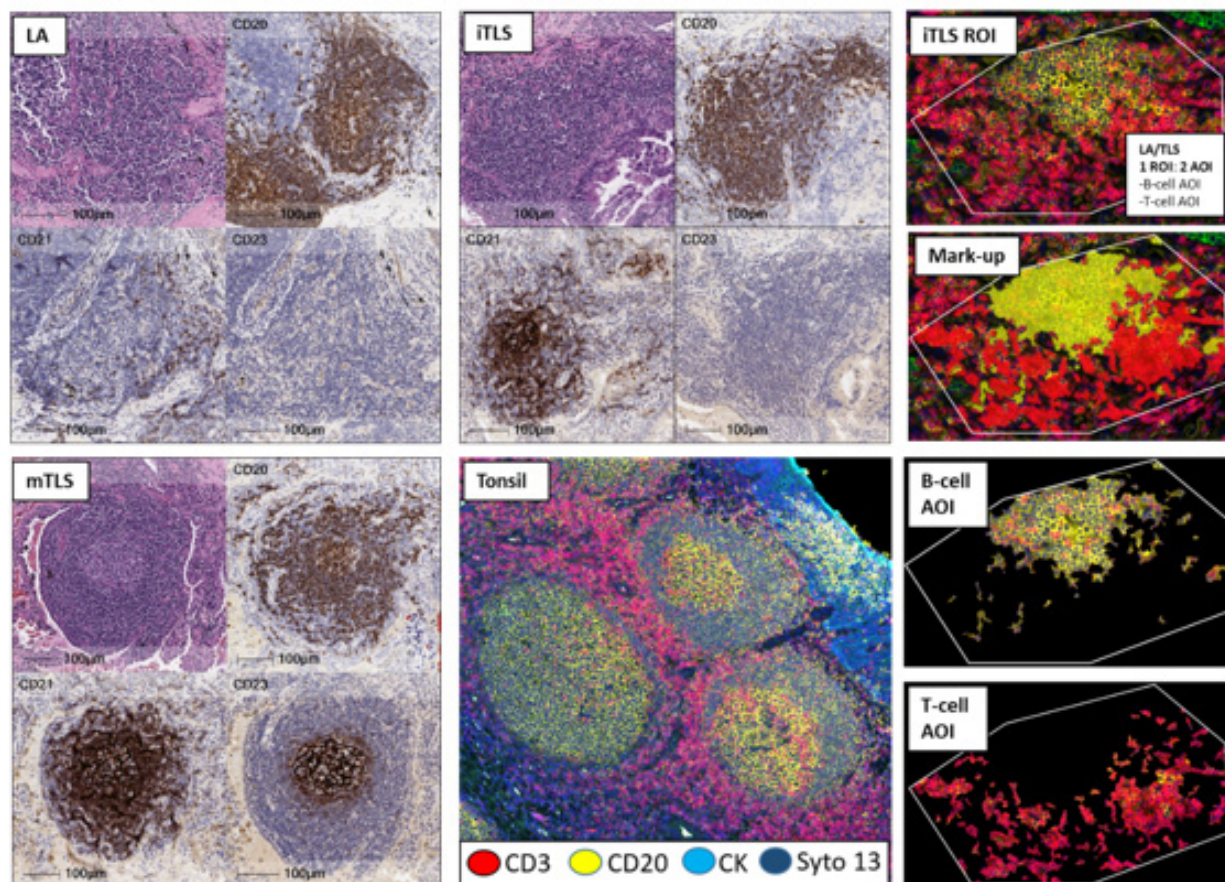
Conclusions: Biomarkers associated with higher antigen presentation and immune cell activation were differentially expressed in B-cell enriched areas of IT mTLS compared to iTLS and LA. IT TLS showed higher immune cell activation and memory profiles compared to AL TLS. These findings provide insights into the stepwise development of TLS and highlight distinct biomarker expression related to tumor presence, warranting further investigation in a larger cohort.

1156 Uncovering Genetic Abnormalities by Optical Genome Mapping Missed by Microarray Analysis in Stillbirth Placental Tissue

Wilfrido Mojica[1], Katherine Mojica[2]
[1]University at Buffalo, SUNY, Buffalo, NY, [2]Keck Graduate Institute, Riggs School of Applied Life Sciences, Claremont, CA

Disclosures: Wilfrido Mojica: None; Katherine Mojica: None

Background: Each advancement in biotechnology results in an improved ability to detect molecular abnormalities that previously may have been missed. High Resolution Microarray analysis (HRMA) has recently supplanted karyotyping as the preferred means of assessing genetic abnormalities in the examination of stillbirths. Innovative technologies like Optical Genome Mapping (OGM) represent the next generation of diagnostic tools poised to become the new state of the art in this field. Herein are presented the first reported results of a side-by-side comparison between HRMA and OGM performed on matching placental tissue from a third trimester stillbirth case.

Design: Unfixed, matched placental tissue was submitted for HRMA and OGM analysis. HRMA was performed using the ISCA 180K oligonucleotide (CGH+SNP) array as a commercially available lab service. Ultra-high-molecular-weight DNA was isolated from the placental tissue and processed via OGM for research purposes and further validation. OGM data analysis was obtained using Access software provided by Bionano Genomics.

Results: The HRMA report indicated that no pathogenic aberrations were identified. High-resolution OGM revealed the presence of 16 insertions, 18 deletions, 1 inversion, 4 duplications, 7 copy number variant (CNV) gain segments after filtering out all polymorphic variants present in Bionano's internal control database. Of the 7 CNVs called with OGM, a relative gain on the X chromosome and a relative loss on the Y chromosome suggest the presence of a mosaic XXY triploidy in this placental tissue sample, which was not indicated in the HRMA report.

Conclusions: Several considerations for the general surgical pathologist are significant in this case. First, it should be articulated that the placenta is no longer considered an ancillary organ but rather, one critical to fetal health and development, and so sampling of it for genetic anomalies is appropriate. Second, the matched pieces of tissue sent for these studies and their disparate findings suggest the possibility that a case of confined placental mosaicism was encountered, and that more placental tissue, as well as fetal tissue should have been sampled. Finally, these results highlight the potential for technologies with higher resolution capabilities over the current state of the art in identifying genetic aberrations; this report may represent the earliest instance of a possible upcoming transition period in this type of testing.

1157 Genomic Landscape Analysis of ERBB3-mutated Human Cancers Reveals Common Co-Occurrence with Activating ERBB2 Alterations

Igor Odintsov[1], Romel Somwar[2], Marc Ladanyi[2]
[1]Brigham and Women's Hospital, Boston, MA, [2]Memorial Sloan Kettering Cancer Center, New York, NY

Disclosures: Igor Odintsov: None; Romel Somwar: None; Marc Ladanyi: None

Background: ERBB3 is a member of the ERBB receptor tyrosine kinase (RTK) family, which includes EGFR, ERBB2 and ERBB4. Gain-of-function point mutations in ERBB3 facilitate direct interactions with other ERBB partners rather than conferring autonomous signaling to this kinase-deficient RTK. The lack of a kinase domain makes ERBB3 an obligate heterodimerization partner, as it mainly acts as an allosteric activator for other ERBB receptors, with consequent activation of downstream signaling and sensitivity to ERBB tyrosine kinase inhibitors *in vitro*. Although *ERBB3* mutations have been reported in multiple tumor types, a comprehensive evaluation of the prevalence of these mutations across cancer types has not been performed. Moreover, given the partner-dependent nature of ERBB3 mutations, investigation of its co-existence with alterations in other ERBB receptors is also pertinent. In this study we describe the prevalence of activating *ERBB3* mutations across human cancers and analyze the genomic landscape of *ERBB3*-mutated tumors.

Design: Retrospective review DNA-based NGS data (January 2014-June 2021) was performed (n=70720 pts). *ERBB3* mutations were annotated as hotspot and/or activating using OncoKB database and current literature.

Results: Out of 70720 patients tested, 582 patients (1%) harbored an activating *ERBB3* alteration. The majority of tumors with ERBB mutations were colorectal, gastric and esophageal cancers, small bowel carcinomas, bladder urothelial carcinomas, uterine endometrioid carcinomas, and breast cancers. Most mutations in ERBB3 occurred in the extracellular domain (85%) with only 15% found in the kinase domain. Concurrent alterations in *ERBB2* were found in 19% of *ERBB3*-altered tumors and were present across the above tumor types (co-enrichment q-value < 0.001), while no significant association was observed for ERBB3 and EGFR (co-enrichment q-value = 0.998).

Conclusions: ERBB3 mutations are potential driver alterations with no FDA-approved therapy. A significant proportion of activating ERBB3 mutations co-occur with activating ERBB2 alterations suggesting synergistic tumorigenic effects. Our work highlights the importance of broad genomic testing to detect *ERBB3* mutations, as these may identify patients potentially responsive to ERBB2 inhibition or antibody-mediated targeting of ERBB3.

1158 Artificial Intelligence-Powered Tumor Purity Assessment From H&E Whole Slide Images Correlates with Consensus Purity Estimation Based on Pathological Examination and Next-generation Sequencing

Gahee Park[1], Sangjoon Choi[2], Seokhwi Kim[3], Soo Ick Cho[4], Wonkyung Jung[5], Jeongun Ryu[5], Minuk Ma[5], Donggeun Yoo[6], Kyunghyun Paeng[6], Chan-Young Ock[6], Sanghoon Song[5], Heon Song[5], Sergio Pereira[6], Seonwook Park[6]

[1]Lunit Inc., Gangnam, South Korea, [2]Samsung Medical Center, Seoul, South Korea, [3]Ajou University School of Medicine, Suwon, South Korea, [4]Lunit Inc., Gang nam gu, South Korea, [5]Lunit Inc., Gangnamgu, South Korea, [6]Lunit Inc., Seoul, South Korea

Disclosures: Gahee Park: *Employee*, Lunit Inc; Sangjoon Choi: None; Seokhwi Kim: None; Soo Ick Cho: *Employee*, Lunit; Wonkyung Jung: *Employee*, Lunit Inc; Jeongun Ryu: *Employee*, Lunit Inc; Minuk Ma: *Employee*, Lunit Inc.; Donggeun Yoo: *Employee*, Lunit Inc.; Kyunghyun Paeng: *Stock Ownership*, Lunit; *Employee*, Lunit; Chan-Young Ock: *Employee*, Lunit Inc.; *Stock Ownership*, Lunit Inc.; Sanghoon Song: None; Heon Song: *Employee*, Lunit Inc; Sergio Pereira: *Employee*, Lunit Inc; Seonwook Park: *Employee*, Lunit Inc.

Background: The advanced genomic analysis capturing tumor-specific profiles in DNA or RNA allowed us to estimate tumor purities more precisely. However, the direct evaluation of tumor purity assessment in a whole slide image (WSI) was limited due to technical challenges. Here, we present an artificial intelligence (AI)-powered tumor purity (AI-P) method using Lunit SCOPE IO to capture and quantify its tumor heterogeneity by defining characteristics of tissue area and cell types from WSI. Furthermore, we implemented AI-P for H&E stained WSI in The Cancer Genome Atlas (TCGA) cohorts to validate previous methodologies of next-generation sequencing (NGS)-based tumor purity estimates.

Design: Lunit SCOPE IO embedded two computer vision models: a tissue segmentation model and a cell detection model to analyze the spatial analysis of heterogeneity on WSI from the pan-cancer analysis. The performance of Lunit SCOPE IO was trained and validated with 3,166 H&E WSI of multiple cancer types, annotated by 52 board-certified pathologists. First, we implemented Lunit SCOPE IO to extract the characteristics of tissue and cell images from H&E stained WSI in TCGA cohorts. The AI-powered tumor purity (AI-P) was calculated as the total number of tumor cell counts in the cancer area over the total cell counts. Next, we evaluated AI-P and differential expression of tumor purity estimates from Aran et al., including breast cancer, lung cancer, and colorectal cancer of TCGA cohorts in 16 cancer types (n= 6,573). Finally, to assess clinical relevance driven by purity estimates in treatment effectiveness and prognosis, we classified AI-P into "high" and "low" by a threshold of 50%.

Results: The overall average tissue size from the TCGA cohorts was 315.3 ± 165.6 (Mean ± SD) mm2 with the average cancer region of 65.9 ± 57.6 (Mean ± SD) mm2 which provided average AI-P estimates of 36.4% ± 18.7% (Mean ± SD). Ovarian cancer had the highest AI-P estimate of 51.2% amongst the 16 cancers. The purity estimates from AI-P and multiple genomic profiling methods (ABSOLUTE, ESTIMATE, and LUMP) had high concordance between most cancer types (|R| > 0.40, p < 0.001), but there was a loose correlation between AI-P and pathologic examination (|R| = 0.18, p < 0.001, Figure 1). Overall survival of the "high" AI-P group (n=1,663) prolonged significantly for those with above 50% of AI-P score compared to the "low" AI-P group (n=4,910, median OS: 85.1 versus 110.9 months, P=0.016). In a subgroup analysis, the "high" AI-P group had significantly poor prognosis in a total of 5 out of 16 cancers (p < 0.05) including kidney clear cell carcinoma (HR 2.26, p = 0.006), uterine corpus endometrial carcinoma (HR 1.71, p = 0.032), colorectal cancer (HR 1.67, p = 0.009), breast cancer (HR 1.47, p = 0.021), and hepatocellular carcinoma (HR 1.45, p = 0.037, Figure 2).

Figure 1 - 1158

Figure 2 - 1158

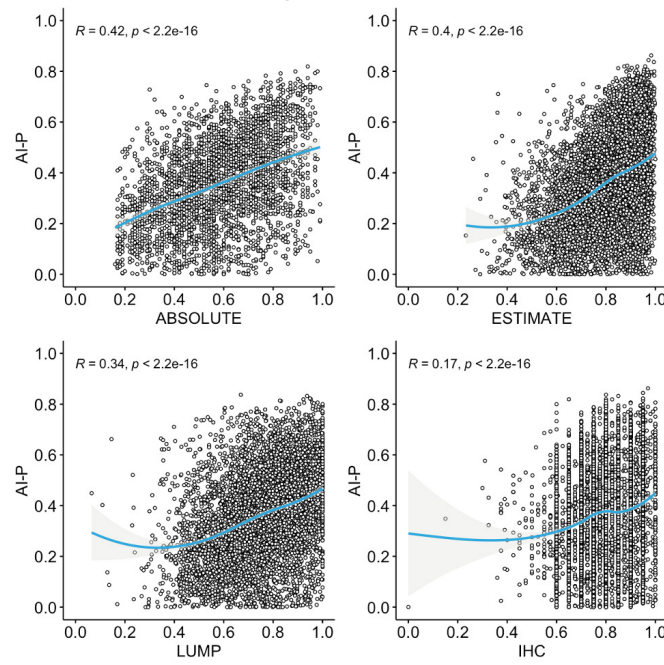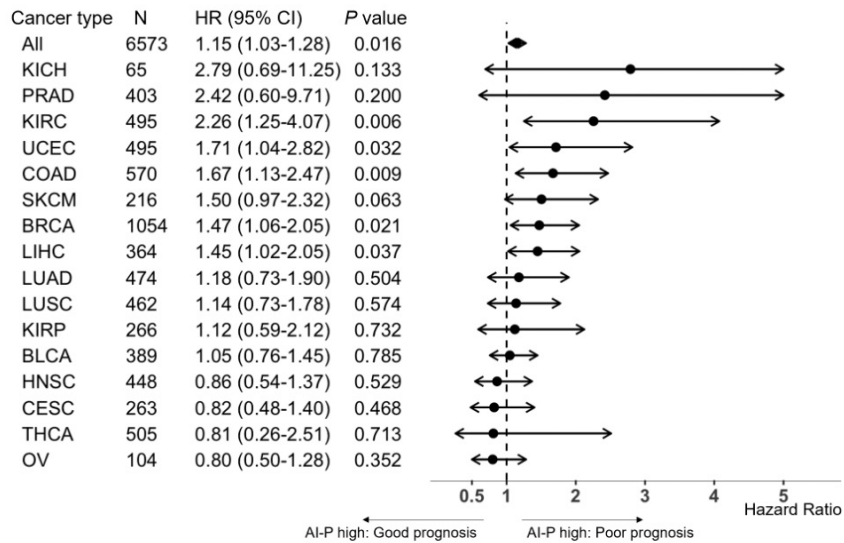| Cancer type	N	HR (95% CI)	P value
All	6573	1.15 (1.03-1.28)	0.016
KICH	65	2.79 (0.69-11.25)	0.133
PRAD	403	2.42 (0.60-9.71)	0.200
KIRC	495	2.26 (1.25-4.07)	0.006
UCEC	495	1.71 (1.04-2.82)	0.032
COAD	570	1.67 (1.13-2.47)	0.009
SKCM	216	1.50 (0.97-2.32)	0.063
BRCA	1054	1.47 (1.06-2.05)	0.021
LIHC	364	1.45 (1.02-2.05)	0.037
LUAD	474	1.18 (0.73-1.90)	0.504
LUSC	462	1.14 (0.73-1.78)	0.574
KIRP	266	1.12 (0.59-2.12)	0.732
BLCA	389	1.05 (0.76-1.45)	0.785
HNSC	448	0.86 (0.54-1.37)	0.529
CESC	263	0.82 (0.48-1.40)	0.468
THCA	505	0.81 (0.26-2.51)	0.713
OV	104	0.80 (0.50-1.28)	0.352

Conclusions: We demonstrated that AI-P provides compatibility of quantifying tumor purity throughout the comparative analysis of genomic-profiled tumor purity measurements. Thus, we believe that using AI-P from Lunit SCOPE IO can practically and expeditiously assess the tumor purity from H&E slides.

1159 Development of a Novel IHC Assay on the BOND-III for Detection of NaPi2b in Serous Ovarian Cancer Samples to Identify Patients Eligible for Treatment with Upifitamab Rilsodotin (UpRi)

Aatish Patel[1], Eric Cowden[1], Nnamdi Okeke[1], Olga Skende[1], Paul Krassnoff[1], Melissa Alexander[2], Rebecca Mosher[3]
[1]Leica Biosystems, Danvers, MA, [2]CT, [3]Mersana Therapeutics, Cambridge, MA

Disclosures: Aatish Patel: *Consultant*, Bristol Myers Squibb; *Employee*, Leica Biosystem; Eric Cowden: None; Nnamdi Okeke: *Employee*, Leica biosystems; Olga Skende: *Employee*, Leica Biosystems; Paul Krassnoff: *Employee*, Leica Biosystems; Melissa Alexander: *Employee*, Leica Biosystems; Rebecca Mosher: *Employee*, Mersana Therapeutics; *Stock Ownership*, Mersana Therapeutics

Background: NaPi2b, a sodium-dependent phosphate transporter protein, is broadly expressed in solid tumors such as serous epithelial ovarian cancer (OC) and non-small cell lung adenocarcinoma with limited expression in healthy tissues. A novel human-rabbit chimeric antibody (Ab) has been formatted for use as an immunohistochemical (IHC) reagent* on the BOND-III autostainer for detection of NaPi2b in formalin-fixed, paraffin-embedded serous ovarian cancer tissue. The NaPi2b (67) Ab is currently under development (IUO) with the intent to be indicated as an aid in identifying OC patients who may have increased probability of clinical benefit following treatment with UpRi, a first-in-class Dolaflexin-based antibody drug conjugate targeting NaPi2b.

Design: An IHC assay system, including scoring guide and controls, was developed on the BOND-III. The assay was performed on 397 commercially procured OC samples. All samples were scored using a ≥75% tumor proportion score (TPS) cut-off to determine frequency of high NaPi2b expressing samples. The H-score for all stained samples was calculated, and the incidence of samples at or above an H-score of 110, a value used in prior publications correlating expression and clinical outcome, was determined. Specificity of the assay was determined by flow cytometry (FC) analysis of well-characterized cell lines and by surveying reactivity in tissue microarrays (TMA) that included various normal and neoplastic tissues.

Results: The frequency of cases above the TPS and H-score cut-offs was similar: 58.9% and 62.5%, respectively. A shift in signal >3 orders was observed by FC when OVCAR3 cells were interrogated by Ab, as compared with a non-expressing cell line. Immunoreactivity was observed in normal tissue and non-ovarian tumor specimens consistent with previously published data.

Conclusions: The NaPi2b (67) assay system demonstrates a broad range of reproducible staining in OC. Current studies indicate that a ≥75% TPS cut-off could be used in a clinical setting for patient selection and identifies a similar population to the previously used H-score. This proposed CDx assay is currently being used in the UPLIFT Study Cohort of UpRi in OC (NCT03319628).

*Assay is Investigational Use Only, not currently approved for diagnostic use.

1160 Pan-cancer Tissue Microarray Analysis Identifies Uroplakin 1b as a Putative Diagnostic Marker in Surgical Pathology

Viktor Reiswich[1], Natalia Gorbokon[1], Franziska Büscheck[1], Andreas Luebke[1], Guido Sauter[1], Ronald Simon[1], Sarah Minner[1], Frank Jacobsen[1], Eike-Christian Burandt[1], Till Clauditz[1], David Dum[1]
[1]University Medical Center Hamburg-Eppendorf, Hamburg, Germany

Disclosures: Viktor Reiswich: None; Natalia Gorbokon: None; Franziska Büscheck: None; Andreas Luebke: None; Guido Sauter: *Grant or Research Support*, MS Validated Antibodies GmbH; Ronald Simon: None; Sarah Minner: None; Frank Jacobsen: None; Eike-Christian Burandt: None; Till Clauditz: None; David Dum: None

Background: Uroplakin 1B (UPK1B) is a structure protein of the urinary bladder urothelium that strengthens the bladder wall to prevent rupture of the urothelium during bladder expansion. Existing RNA expression data suggest that physiologic UPK1B expression is limited to only a few normal tissue types.

Design: To comprehensively evaluate the potential diagnostic and prognostic utility of Upk1b expression analysis, a tissue microarray containing 15,182 samples from 127 different tumor types and subtypes and 608 samples of 76 different normal tissue types was analyzed by immunohistochemistry.

Results: Positive staining for UPK1B was found in 61 (48%) different tumor types. At least one moderately positive tumor was seen in 50 (39%) tumor types, and 39 tumor types (31%) had at least one strongly positive tumor. Most frequent and strongest expression was found in urothelial neoplasms (58-95%), Brenner tumors of the ovary (92%), epitheloid mesothelioma (87%),

serous carcinomas of the ovary (58%) and the endometrium (53%) as well as squamous cell carcinomas of various sites of origin. UPK1B staining was rare in lung adenocarcinoma (6.8%) and largely absent in colorectal (0.7%) or prostatic adenocarcinoma (1.3%). In urothelial tumors cancer, low Upk1b expression was linked to high grade and invasive tumor growth (p<0.0001 each) as well as nodal metastasis (p=0.0006).

Conclusions: In conclusion, our data show that UPK1B analysis supports the differential diagnosis of malignant mesothelioma vs. adenocarcinoma of the lung, urothelial carcinoma vs. prostatic adenocarcinoma in the bladder, or pancreatico-biliary and gastro-esophageal vs. colorectal adenocarcinomas.

1161 Stimulated Raman Spectroscopy as Rapid On-site Evaluation of Renal Neoplastic and Non-neoplastic Biopsies

Joyce Ren[1], Miles Mannas[1], Derek Jones[2], Daniel Orringer[1], Samir Taneja[1], Fang-Ming Deng[3]
[1]NYU Langone Health, New York, NY, [2]NYU Langone Medical Center, New York, NY, [3]New York University Medical Center, New York, NY

Disclosures: Joyce Ren: None; Miles Mannas: None; Derek Jones: None; Daniel Orringer: None; Samir Taneja: None; Fang-Ming Deng: None

Background: Image guided renal biopsy plays an important role in the diagnoses of neoplastic and non-neoplastic renal diseases. The contemporary rate of non-diagnostic renal biopsy ranges from 15-18% though may be as high as 42% in challenging cases. Simulated Raman Histology (SRH) is a novel microscopic technique which creates rapid high-resolution images of unprocessed tissue which may be viewed on standard radiology viewing platforms at the time of the procedure to provide rapid on-site evaluation (ROSE) of sample adequacy and preliminary interpretation. SRH may thus reduce the rate of non-diagnostic biopsy, avoid potential complications from additional procedures, and provide pathologic information that may have immediate implications on clinical management. We evaluated our initial experimental application of SRH as ROSE of renal biopsies.

Design: An *ex vivo* 18-gauge core needle biopsy was taken from a series of radical or partial nephrectomy specimens. Two cores of tumor and two cores of adjacent non-neoplastic renal parenchyma were collected from each case. Images of the fresh unstained biopsy samples were generated using a SRH microscope using two Raman shifts: 2845cm^{-1} and 2930cm^{-1}. The cores were then processed as per routine H&E protocols. The SRH and H&E images were reviewed by a genitourinary pathologist.

Results: The SRH microscope took 8-11 minutes to produce images of the renal biopsies. Non-neoplastic renal parenchyma and four distinct RCC subtypes were captured (Table 1). Examples of the high-quality SRH images are shown in Figures 1 and 2 in comparison to H&E images. Non-neoplastic renal structures and areas of tumors were easily recognized on SRH images and correlated well with their corresponding H&E sections. The H&E sections showed no significant changes in their quality after SRH microscopy.

Table 1: Renal cell carcinoma (RCC) subtypes biopsied *ex vivo* for visualization with Stimulated Raman Histology	
RCC subtype	**Number of Cases**
Clear cell	7
Chromophobe	3
Papillary	2
Renal Medullary	1

Figure 1 - 1161

Figure 2 - 1161
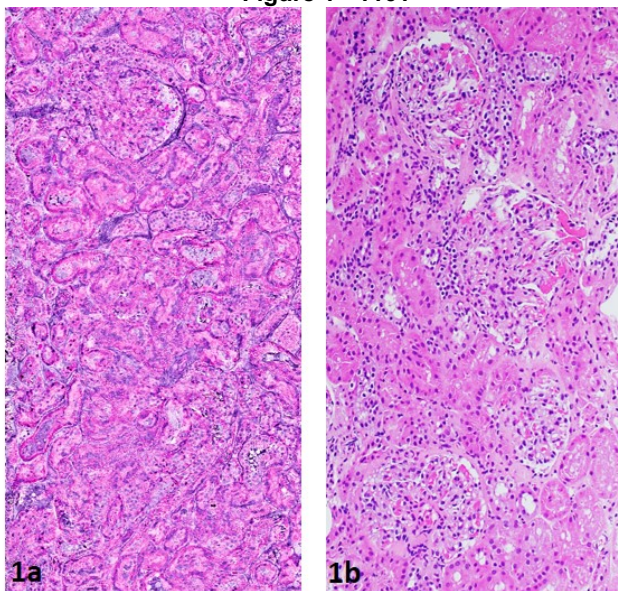

Figure 1. 1a) SRH-generated normal renal parenchyma
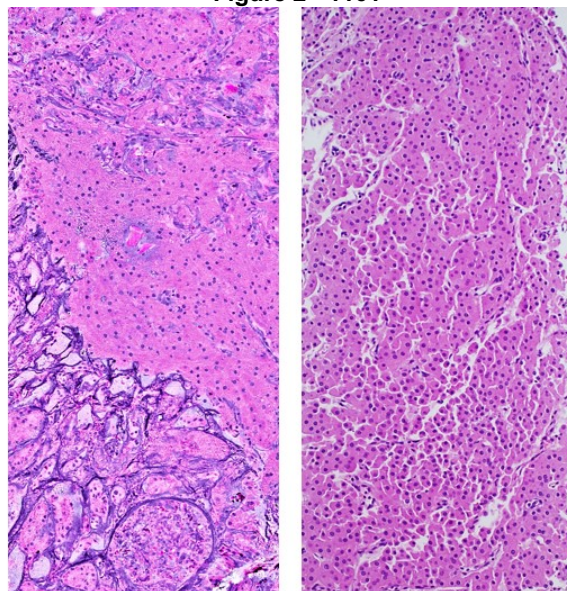1b) H&E of normal renal parenchyma

Figure 2. 2a) SRH-generated Chromophobe RCC
2b) H&E of Chromophobe RCC

Conclusions: SRH generates high quality images of benign renal parenchyma and tumors which can be rapidly produced and easily interpreted at the time of the biopsy to determine biopsy adequacy. The quality of the tissue biopsy material is not compromised and remained available for routine histologic processing and immunohistochemistry assays for confirmation of histologic diagnosis. SRH can expedite the diagnosis and help to stratify the malignancy risks of renal lesions in diagnostically challenging cases. Furthermore, decisions to obtain additional tissue for immunohistochemistry, molecular, and genetic ancillary studies can be made at the time of the procedure if indicated.

1162 A Comparison Between Manual and Automated Instrumentation Evaluations Using ihcDirect Antibodies

Sarah Richardson[1], Jianfu Wang[1], Justin Jefferson[2], Shuo Chen[1]
[1]Novodiax, Inc, Hayward, CA, [2]Novodiax, Inc, Austin, TX

Disclosures: Sarah Richardson: *Employee*, Novodiax, Inc.; Jianfu Wang: None; Justin Jefferson: None; Shuo Chen: None

Background: New approaches to increase the volume of IHC slides tested while decreasing laboratory time spent on manual application of IHC protocols has led pathologists to introduce the automated process into their laboratories. Automation of the IHC procedure can overcome insufficient human resources and significantly improves laboratory efficiency in terms of test turnaround time. The demand for rapid automated IHC testing by laboratories is routinely seen for frozen intraoperative surgeries such as in Mohs micrographic surgery (MMS) and other applications.

Design: In the present study, we aim to demonstrate the utility of polyHRP conjugated SOX10 and Pan-CK antibodies using manual and automated methods. Anti-SOX10 is a biomarker that is diagnostically used to identify melanoma during extraction of malignant tissue. Pan-CK is a cytokeratin marker used clinically for breast cancer diagnosis and micrometastasis detection. Using anti-SOX10 and anti-Pan-CK, we tested frozen skin (normal and melanoma) and breast cancer tissue using manual staining with a comparison to the Leica Bond III as well as our novel Q-STAIN®X (QSX) autostainer.

Results: The manual staining was completed in less than 15 minutes demonstrating increased testing efficiency compared to conventional IHC techniques. QSX staining was completed in less than 20 minutes providing results while SOX10 and Pan-CK testing with the Leica autostainer was completed in less than 40 minutes. All tissues tested demonstrated equivalent staining quality based on pathologist review and grading across all three methods.

Conclusions: The rapid QSX test turnaround time and minimal hands-on time as well as consistent staining quality support its use for clinical intraoperative applications. Results indicate the diagnostic utility of rapid automated IHC in intraoperative testing as seen with anti-SOX10 and anti-Pan-CK to aid in the rapid identification of target cells and antigens for diagnostic purposes. Additionally, the rapid QSX test turnaround time facilitates its use clinically for intraoperative applications.

1163 Enteric Gliosis and Neuronal Loss in Crohn's Intestinal Segmental Strictures

Jason Siu[1], Yuan Lin[2], Fang Li[2], Wenhui Hu[2], Xianyong (Sean) Gui[3]
[1]University of Washington, Seattle, WA, [2]Temple University Medicine, Philadelphia, PA, [3]University of Washington Medical Center, Seattle, WA

Disclosures: Jason Siu: None; Yuan Lin: None; Fang Li: None; Wenhui Hu: None; Xianyong (Sean) Gui: None

Background: Intestinal segmental stricture (SS) is the most common complication of Crohn's disease (CD) and bottleneck in treatment. To elucidate its pathogenic mechanisms and identify potential therapeutic targets are urgently needed. Histologically, transmural muscular hyperplasia/hypertrophy is the most prominent change in CD-SS, which is frequently accompanied by myenteric and submucosal ganglion (MG/SMG) hyperplasia. We suspect a dysregulated neuromuscular remodeling in response to localized deep inflammation as the key pathologic process in CD-SS, and we studied preliminarily the changes of enteric neuronal cells (ENCs) and glial cells (EGCs) in the involved bowel wall.

Design: Full-thickness cross sections of bowel wall (terminal ileum 14, colon 6) within the strictures were taken from 20 surgical resection specimens of patients with CD-SS. Similar sections of adjacent inflamed but non-stricture bowel and healthy region were paired for each case as controls. The number/density and size of MG and SMG were measured microscopically on H&E slides. ENCs and EGCs were identified by immunohistochemistry and multilabeled immunofluorescence using antibodies for NeuN and HuD (both marking ENCs) as well as S100β and GFAP (both marking EGCs) on paraffin-embedded tissue blocks, and their number/density within MGs and SMGs were counted by manual microscopic reading and multicolor confocal image analysis.

Results: In the bowel wall involved by CD-SS, MG hyperplasia (increased number) and hypertrophy (increased size) were common. The number of MGs (per 10× field) was almost twice of that in healthy bowel (7.48±2.89 vs. 3.34±0.76, p=0.0028), and meanwhile the number of ENC-containing MGs decreased significantly (41% vs 63%, p=0.00007). SMGs also increased significantly than that in non-stricture and healthy regions. Both S100β+ and GFAP+ EGCs, individual- and dual-expression, were significantly increased in MGs as well as SMGs, while HuD+ ENCs decreased, as compared to non-stricture and healthy controls (p<0.0001) (as shown in representative figures). Significant differences between non-stricture and healthy bowel also existed.
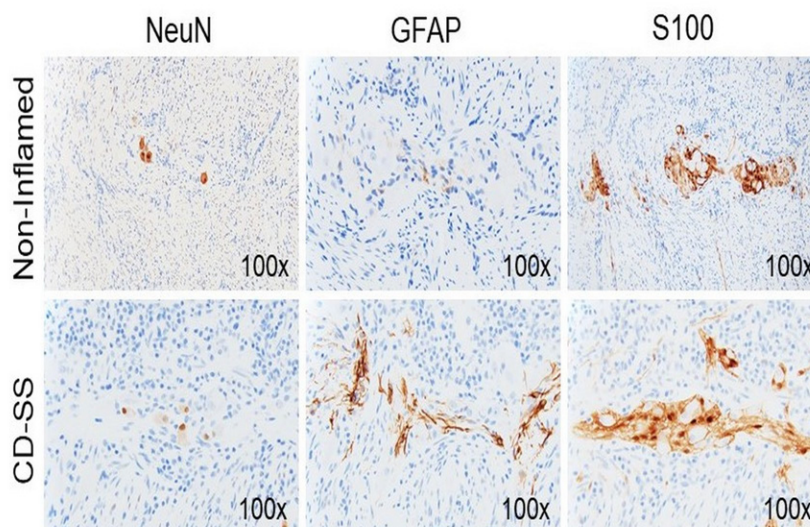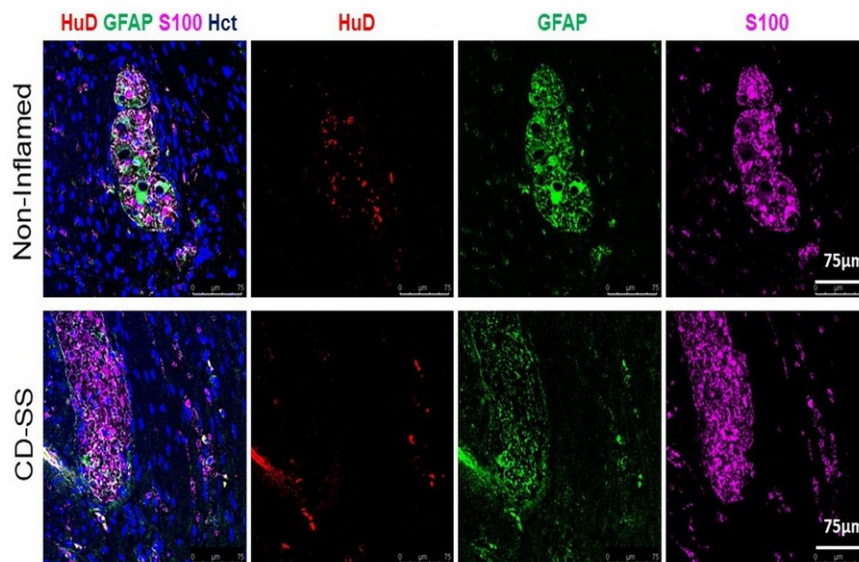
Figure 1 - 1163

Figure 2 - 1163

Conclusions: Our data demonstrated enteric neuronal loss and gliosis occurred in muscularis propria and submucosa in CD-SS, which may be associated with the intestinal smooth muscle cell (ISMC) hyperplasia as a dysregulated ISMC-ENS (enteric nervous system) network affected by inflammatory mediators in Crohn's transmural inflammation.

1164 Proteomic Landscape of Pancreatic Neuroendocrine Tumors

Atsushi Tanaka[1], Makiko Ogawa[1], Kei Namba[1], Ronald Hendrickson[1], David Klimstra[1], Michael Roehrl[1]
[1]Memorial Sloan Kettering Cancer Center, New York, NY

Disclosures: Atsushi Tanaka: None; Makiko Ogawa: None; Kei Namba: None; Ronald Hendrickson: None; David Klimstra: None; Michael Roehrl: None

Background: Little is known about the deep pan-proteomic approaches to pancreatic tumors. Previous transcriptome studies have likely missed targetable proteins because global correlation between mRNA abundance and quantitative protein expression is generally low. This encouraged us to perform deep mass spectrometric pan-proteomic analyses of pancreatic neuroendocrine tumors (PanNETs) and to identify protein biomarkers that are specific to them.

Design: We selected 20 PanNETs and 20 ductal adenocarcinomas (PDAC) as a comparison group. We also analyzed 40 benign pancreatic tissues. Total proteomes were extracted from flash frozen tissue and analyzed by liquid chromatography tandem mass spectrometry using a high-resolution Orbitrap Fourier transform instrument. Protein identification and expression profiling were performed with MaxQuant software using label-free quantification. We performed unsupervised classification, differential expression analysis, and protein pathway enrichment analysis. To uncover possible therapeutic vulnerabilities of PanNETs, we searched drug-protein interactions by using the drug-gene interaction database (DGIdb).

Results: We detected 8,544 proteins in these samples. We found specific proteins for each group (i.e., benign, PanNET, and PDAC), ranging from 183 to 271 proteins. Unsupervised clustering of all lesions clearly separated each entity. We performed differential expression analysis and pathway enrichment analysis and found over 400 up-regulated proteins and 250 down-regulated proteins. Pathway analysis showed not only classical oncogenic pathway enrichment but also metabolic pathway enrichment, shedding light onto interesting biological energy production mechanisms of PanNETs. Unsupervised clustering of PanNETs revealed distinct proteomic subtypes within. These findings provide cues for the development of better outcome risk prediction and treatment of PanNETs. DGIdb searches identified over 100 targetable proteins in PanNET.

Conclusions: Global deep proteomics by mass spectrometry characterizes proteomic landscapes of PanNETs and defines proteomic tumor subtypes. Our approach may provide better classification methods, understanding of oncogenesis, and potential prognostic biomarkers that are specific to this rare pancreatic tumor. Proteomics may enable us to tailor the treatment of these tumors and would provide solutions for analogous problems in many other cancer types.

1165 Suitability of Combined Immunohistochemistry Analysis of CPA1 and CELA3B for Diagnosing Acinar Cell Carcinoma of the Pancreas

Ria Uhlig[1], Hendrina Contreras[1], Nina Bröker[1], Soeren Weidemann[2], Natalia Gorbokon[1], Anne Menz[1], Maximilian Lennartz[1], Viktor Reiswich[1], Guido Sauter[1], Waldemar Wilczak[1], Sarah Minner[1], Stefan Steurer[3], Eike-Christian Burandt[1], David Dum[1], Ronald Simon[1], Till Krech[1], Till Clauditz[1], Frank Jacobsen[1]

[1]University Medical Center Hamburg-Eppendorf, Hamburg, Germany, [2]University Hospital Hamburg, Hamburg, Germany, [3]University Medical Center Hamburg-Eppendorf, Germany

Disclosures: Ria Uhlig: None; Hendrina Contreras: None; Nina Bröker: None; Soeren Weidemann: None; Natalia Gorbokon: None; Anne Menz: None; Maximilian Lennartz: None; Viktor Reiswich: None; Guido Sauter: *Grant or Research Support*, MS Validated Antibodies GmbH; Waldemar Wilczak: None; Sarah Minner: None; Stefan Steurer: None; Eike-Christian Burandt: None; David Dum: None; Ronald Simon: None; Till Krech: None; Till Clauditz: None; Frank Jacobsen: None

Background: Carboxypeptidase A1 (CPA1) and chymotrypsin-like elastase family member 3B (CELA3B) are pancreatic enzymes with specific roles for nutrient digestion. Immunohistochemistry analyses suggest that both proteins are secreted from pancreatic acinar cells.

Design: To assess the utility of immunohistochemical co-analysis of CPA1 and CELA3B for the diagnosis of acinar cell carcinoma, a tissue microarray containing 13,618 samples from 129 different tumor types was analyzed by immunohistochemistry.

Results: Of 10,334 interpretable tumors, 5 (0.05%) were positive only for CELA3B, 2 (0.02%) only for CPA1, and 12 (0.12%) for both proteins. Of these 19 tumors, 14 (75%) were acinar cell carcinomas of the pancreas, 1 (5%) was an acinar cell carcinoma of the salivary gland, and 2 (10%) each were mucoepidermoid carcinomas of the salivary gland and adenocarcinomas of the colon. Of the 14 pancreatic acinar cell carcinomas, 12 were positive for CPA1 and CELA3B, and 2 were positive for CELA3B only. For CPA1 alone, the sensitivity and specificity for the detection of acinar cell carcinomas was 85.7% and 100%. For the combined analysis of CPA1 and CELA3B, the sensitivity and specificity for the detection of acinar cell carcinomas was 100% and 99.9%.

Conclusions: In conclusion, the combined analysis of CPA1 and CELA3B enables for highly sensitive diagnosis of acinar cell carcinomas of the pancreas.

1166 A Nanotechnology-enabled, Extracellular Vesicle-based Assay for Reflecting Progression of Prostate Cancer

Jasmine Wang[1], Na Sun[2], Yi-Te Lee[2], Minhyung Kim[1], Jie-Fu Chen[3], Sungyong You[1], Yazhen Zhu[4], Hsian-Rong Tseng[2], Edwin Posadas[1]

[1]Cedars-Sinai Medical Center, Los Angeles, CA, [2]David Geffen School of Medicine at UCLA, Los Angeles, CA, [3]Memorial Sloan Kettering Cancer Center, New York, NY, [4]University of California, Los Angeles, Los Angeles, CA

Disclosures: Jasmine Wang: None; Na Sun: None; Yi-Te Lee: None; Minhyung Kim: None; Jie-Fu Chen: None; Sungyong You: None; Yazhen Zhu: None; Hsian-Rong Tseng: *Stock Ownership*, CytoLumina Technologies Corp; Edwin Posadas: *Speaker*, Myovant, Bayer, Genentech

Background: With the expansion of therapeutics strategies in prostate cancer (PCa), there is an unmet need to develop a minimally invasive assay, for example, liquid biopsy, to detect the metastatic progression of PCa patients for timely treatment. Our team pioneered a novel Extracellular Vesicle (EV) Digital Scoring Assay, which integrates a microfluidic device for purification of tumor-derived EVs and reverse transcription-droplet digital polymerase chain reaction for quantification of RNAs from the purified EVs. On the basis of our previous success, we aim to optimize this assay for PCa and conduct a pilot study to assess the performance of this assay in reflecting the disease status over the natural history of PCa.

Design: The conditions of EV Digital Scoring Assay for PCa were optimized using 22Rv1-derived EVs. To develop a gene panel for reflecting disease status of PCa, 11 prostate lineage specific mRNA markers were selected from databases and were validated using PCa cell lines and EVs. Plasma from 20 localized and 20 metastatic PCa patients were subjected to this assay in conjunction with the 11-gene panel. Serial plasma from three PCa patients were tested to evaluate the performance of dynamic monitoring. mRNA expressions were computed using weighted Z score method and the performance of the assay was evaluated using ROC curve.

Results: With the optimized conditions of anti-EpCAM and anti-PSMA antibodies to capture PCa-derived EVs, the capture efficiency of PCa EV Digital Scoring Assay outperformed ultracentrifugation or ExoQuick-TC™ Exosome Precipitation Solution. A 11-gene panel consisting of *ACP3, FOLH1, HOXB13, KLK2, KLK3, KLK4, MSMB, RLN1, SLC45A3, STEAP2,* and *TMPRSS2* was selected and validated by PCa cell lines-derived EVs. In the clinical pilot study, the Z scores calculated from the expressions of this 11-gene panel are significantly different between 20 localized PCa and 20 metastatic PCa patients (P<0.001) with an area under the ROC curve (AUROC) of 0.88 (P<0.001) which surpassed the power of PSA (AUROC = 0.64) (Figure 1). Longitudinal analysis of 3 PCa patients showed that the Z scores can reflect the clinical progression, response, and stable status respectively, even at a low disease burden that is undetectable by PET.

Figure 1 - 1166
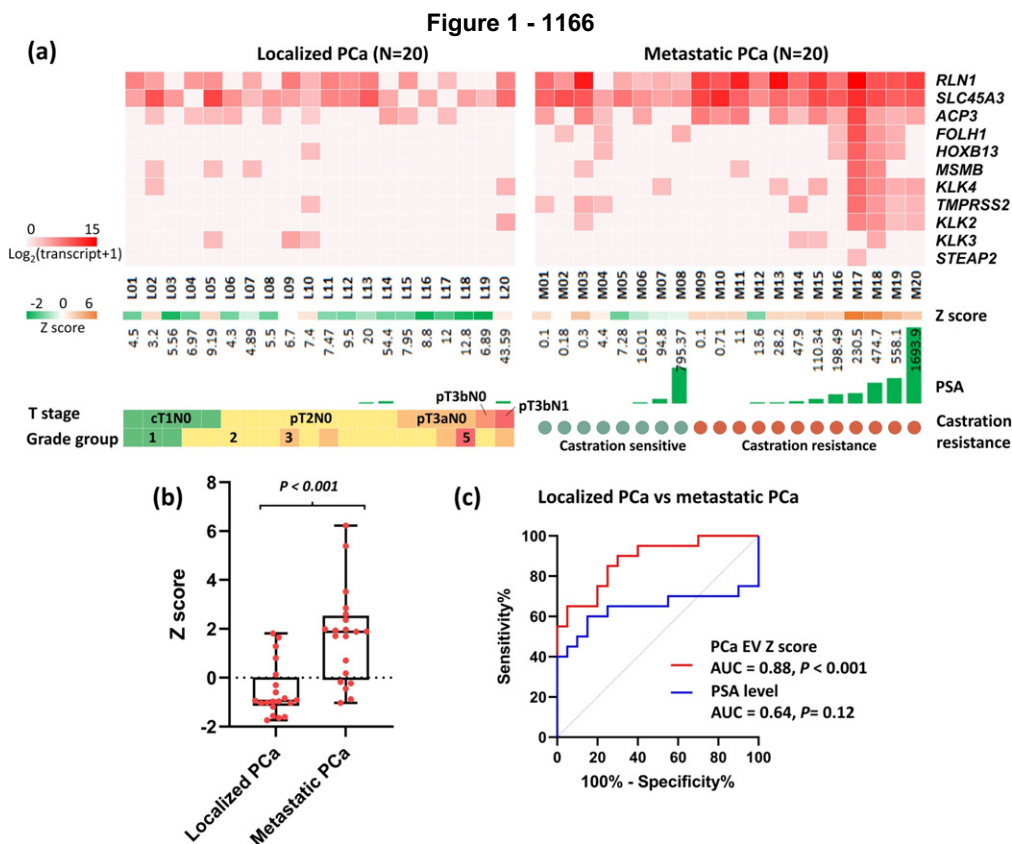
Conclusions: We describe a sensitive PCa EV Digital Scoring Assay to characterize EV-derived mRNA signatures of 11 prostate lineage-specific genes. The resulting EV Z score can distinguish metastatic from localized PCa patients and can reveal the dynamic disease states of PCa patients when being tested longitudinally. This assay may offer the opportunity to complement current imaging tools and PSA for timely detection of metastatic progression and thereby optimize the care for PCa patients.

1167 CD1C was Identified as a Potential Biomarker by the Comprehensive Exploration of Tumor Mutational Burden and Immune Infiltration in Diffuse Large B Cell Lymphoma

Xiaoyu Xiang[1], Li-min Gao[1], Yuehua Zhang[1], Wen-yan Zhang[1]
[1]West China Hospital, Sichuan University, Chengdu, China

Disclosures: Xiaoyu Xiang: None; Li-min Gao: None; Yuehua Zhang: None; Wen-yan Zhang: None

Background: Tumor mutational burden (TMB) is a useful biomarker to predict prognosis. This study was to explore the prognostic value of TMB and the potential association between TMB and immune infiltration in DLBCL.

Design: We downloaded the gene expression profile, somatic mutation and clinical data of DLBCL patients from the Cancer Genome Atlas (TCGA) database. TMB was calculated and we classified the samples into high- and low-TMB group in order to identify differentially expressed genes (DEGs). Functional enrichments analyzes were performed to identify the biological function

of the DEGs. Besides, we utilized the CIBERSORT algorithm to estimate the abundance of 22 immune fractions, and the significant difference were determined by Wilcoxon rank-sum test between high- and low-TMB group. Hub gene had been screened as the prognostic TMB-related immune biomarker by the combination of the Immunology Database and Analysis Portal (ImmPort) database and the univariate Cox analysis from the Gene Expression Omnibus (GEO) database including three DLBCL datasets. Various database application (TIMER, CellMiner, knockTF, GETx) verified the functions of target gene.

Results: SNP occurred more frequently than insertion and deletion, and C > T was the most common of SNV in DLBCL. Survival analysis showed that high-TMB group conferred poor survival outcomes. A total of 62 DEGs were obtained and 13 TMB-related immune genes were identified. Univariate Cox analysis result illustrated that CD1C mutation was associated with lower TMB and manifested a satisfactory clinical prognosis by analysis of large samples from GEO database. In addition, infiltration levels of immune cells in high-TMB group were lower. Using the TIMER database, we further systematically analyzed the relationships between mutants of *CD1C* and immune infiltration levels. Drug sensitivity showed that there was a significant correlation between *CD1C* expression level and clinical drug sensitivity from CellMiner database. KnockTF database was used to comprehensively explore the regulation of gene-related transcription factors and signaling pathways. We searched the GETx database to compare the mRNA expression levels of *CD1C* between lymphoma and normal tissues and the results suggested that there was significant difference between tumor and normal tissues in most studies.

Target Gene	TF	Knock-Method	Tissue Type	Biosample Name	Fold Change	Log2FC
CD1C	CREB1	shRNA	Haematopoietic and lymphoid tissue	K562	0.43886	-1.18818
CD1C	AHR	siRNA	Haematopoietic and lymphoid tissue	THP-1	0.36694	-1.4464
CD1C	TOX	shRNA	Haematopoietic and lymphoid tissue	CCRF-CEM	0.32445	-1.62392

Figure 1 - 1167

Figure1:Workflow

Figure 2 – 1167

Altered in 36 (97.3%) of 37 samples.

Missense_Mutation   **Splice_Site**

Frame_Shift_Ins   **Translation_Start_Site**

Nonsense_Mutation   **In_Frame_Ins**

In_Frame_Del   **Multi_Hit**

Frame_Shift_Del

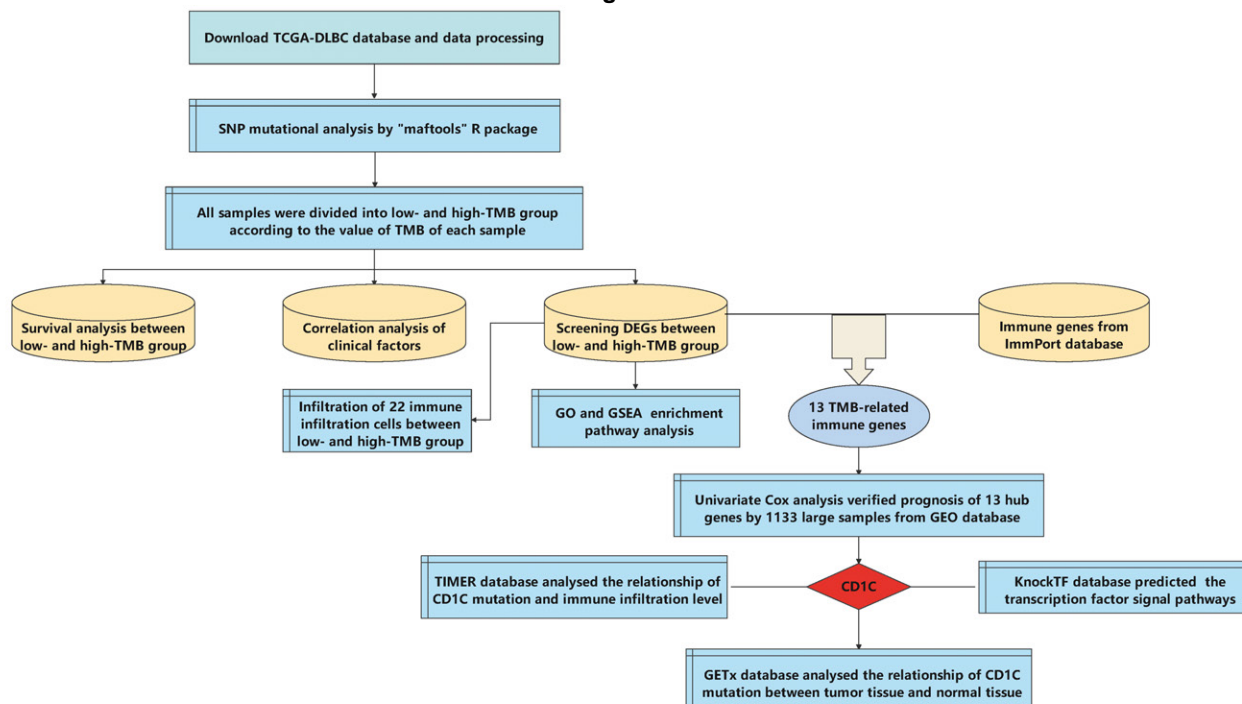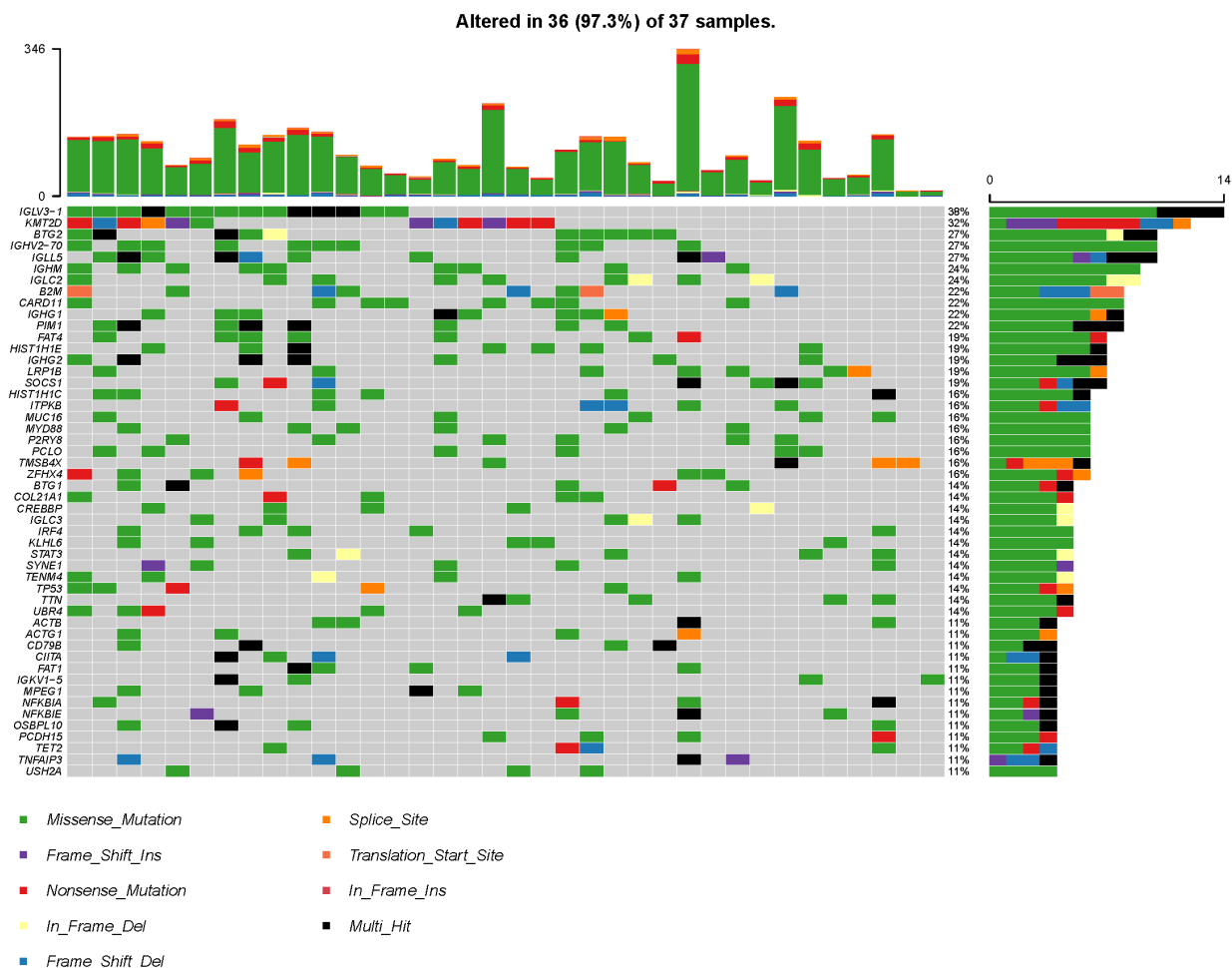**Conclusions:** Higher TMB correlated with poor survival outcomes and might inhibit the immune infiltrates in DLBCL. Our results suggest that *CD1C* is a TMB-related prognostic biomarker.

1168   Multi-cancer Evaluation of Multiplex Immune Markers Using Digital Image Analysis in Patients Treated with Immune Checkpoint Inhibitors

Henry Xie[1], Ekaterina Olkhov-Mitsel[2], Jennifer Du[3], Martin Smoragiewicz[4], Elzbieta Slodkowska[3], Michelle Downes[2]
[1]University of Toronto, Toronto, Canada, [2]Sunnybrook Health Sciences Centre, Toronto, Canada, [3]Sunnybrook Health Sciences Centre, University of Toronto, Toronto, Canada, [4]Sunnybrook Health Sciences Centre, Odette Cancer Centre, Toronto, Canada

Disclosures: Henry Xie: None; Ekaterina Olkhov-Mitsel: None; Jennifer Du: None; Martin Smoragiewicz: None; Elzbieta Slodkowska: None; Michelle Downes: None

Background: Heterogeneous tumor response has been reported in cancer patients treated with immune checkpoint inhibitors (ICIs). This study investigated key markers of activated cytotoxic T lymphocytes (CD8, GzB), immune suppression (FOXP3) and immune escape (loss of MHC I) in association with response to ICIs. To overcome the limited quantities of tumor in biopsy material we developed a multiplex immunohistochemistry (m-IHC) panel with digital workflow.

Design: 19 high grade urothelial cancer (HGUC) and 13 head and neck squamous cell carcinoma (HNSCC) cases treated with PD-1 and PD-L1 inhibitors were identified. MHC I IHC was performed on pre-treatment specimens and scored as follows: positive >75%; reduced 25-75%; and negative <25% of staining. PD-L1 staining (22C3) was scored using cancer specific

algorithms. Subsequently, an inhouse tri-chromogen m-IHC assay consisting of CD8, GzB and FOXP3 analysis was performed. Whole scanned slide images (WSI) and 4 manually annotated hotspot regions of interest (ROI) were analyzed using QuPath version 0.2.3 open-source software. m-IHC was scored as number of positive cells/mm2 for each marker, using an object quantification algorithm. Progression free survival (PFS) was identified using imaging modalities. Overall survival (OS) was defined as death from disease.

Results: Scoring of ROIs was significantly concordant with WSI scoring (all p<0.001) while also being more practical, time-effective and decreasing computational complexity. CD8 and GzB expression were significantly correlated (Pearson correlation coefficient: 0.909, P<0.001). There was a trend towards reduced PFS and OS in negative vs. reduced MHC I IHC (HR=1.3, 95%CI 0.355-4.712 and HR= 4.086, 95%CI 0.522-32.005, respectively) which did not reach statistical significance (p>0.05) likely due to cohort size. There was no significant correlation between PD-L1, CD8, GzB, or FOXP3 and PFS or OS. CD8 expression was higher in MHC I positive cases (median 510 cells/mm2) vs. cases with reduced (median 155 cells/mm2) and negative (median 135 cells/mm2) MHC I expression.

Conclusions: Opportunities exist for novel and complimentary predictive immune biomarkers for ICI therapy using m-IHC and computer assisted digital WSI. Here, we summarize the inter-individual variations in key immune markers in HGUC and HNSCC to increase our understanding of the tumor immune microenvironment. Accrual of an expanded cohort of patients is planned to further investigate prognostic immune biomarkers for ICI therapy.

1169 Targeting TAT-hOGG1 into Mitochondria as a Therapeutic Strategy for Breast Cancer Progression

Larysa Yuzefovych[1], Viktor Pastukh[1], Andrea Kahn[2], Lyudmila Rachek[1]
[1]University of South Alabama College of Medicine, Mobile, AL, [2]The University of Alabama at Birmingham, Birmingham, AL

Disclosures: Larysa Yuzefovych: None; Viktor Pastukh: None; Andrea Kahn: None; Lyudmila Rachek: None

Background: Previously, using a genetic model of breast carcinoma (BC) (PyMT mouse), we have obtained proof-of-concept results that mitochondrial DNA (mtDNA) damage regulates BC **progression. In the current study we utilized a translational strategy** of TAT-protein transduction system to target the recombinant DNA repair enzyme human OGG1 directly into mitochondria of breast cancer cells.

Design: We have used intraperitoneal (IP) injections every other day of active/mutant 10 mg/kg of TAT-hOGG1 or vehicle to PDX and PyMT mice. For the PyMT mice, we have used "prevention" and treatment of established tumor ("cure") model. For prevention model**,** six week old PyMT female mice were injected and for treatment of established tumor model we have started IP injections at a later time (~12 weeks) when most of the mammary tumors were palpable. At the end of the study, mice were euthanized and their mammary tumors were carefully excised and weighed. The total tumor weight per mouse was recorded. The tissue was fixed in formalin, paraffin embedded, and stained with hematoxylin-eosin. Lungs from both mice models were evaluated for metastases and number of metastatic foci recorded. mtDNA/nuclear DNA ratio and oxidative mtDNA damage were evaluated in primary tumors using qRT-PCR and Quantitative Southern blot, respectively.

Results: PDX mice injected with active or mutant TAT-hOGG1 developed significantly smaller tumors and showed a tendency to increase mtDNA copy number compared to vehicle. Moreover, oxidative mtDNA damage was diminished in tumors isolated from mice injected with active TAT-hOGG1 compared to both mutant enzyme and vehicle injected mice. PyMT mice injected with active or mutant TAT-hOGG1 (cure model) developed significantly smaller tumors and show a tendency to decrease number of lungs metastases compared with PyMT mice injected with vehicle. In the prevention model, mitochondrial targeting of active and mutant TAT-hOGG1 reduced tumor weight while increasing lungs metastases compared to mice injected with vehicle although the difference was not statistically significant. In both PyMT models, mtDNA content and oxidative mtDNA damage was increased in vehicle treated mice compared to mice treated with active enzyme.

Conclusions: Our data provides strong rationale to use TAT-delivery of DNA repair enzymes into mitochondria as a new translational approach for treatment of breast cancer.

1170 Computer-aided Detection of Adenoid Cystic Carcinoma in Whole Slide Images

Fanlin Zhou[1], Yu Li[2], Xiaoju Li[3], Jianing Fan[4], Fang Liu[1]
[1]Chongqing University Cancer Hospital, Chongqing, China, [2]Chongqing University Cancer Hospital, Guangzhou, China, [3]Chongqing, China, [4]Chongqing University Cancer Hospital, China

Disclosures: Fanlin Zhou: None; Yu Li: None; Xiaoju Li: None; Jianing Fan: None; Fang Liu: None

Background: The diagnosis of Adenoid cystic carcinoma (ACC) and basal cell adenoma (BCA) depends on pathological sections and immunohistochemistry. However, human evaluation of pathological sections is highly dependent on the experience of pathologists, therefore, it is sometimes difficult to distinguish between these two kinds of tumors in terms of pathomorphology. In order to distinguish the two tumors more accurately and efficiently, we used digital pathology and deep learning to improve the objectivity and efficiency of histopathologic slide analysis.

Design: 400 cases of Salivary Gland between August 2017 and August 2020 in our institution were used to train our model(n=320) and the test set(n=80). All histologic diagnoses were originally made by pathologists from the Chongqing University Cancer Hospital (Chongqing, China). Firstly, 214 cases of adenoid cystic carcinoma and 186 cases of basal cell adenoma were stained with hematoxylin-eosin(H&E). Secondly, H&E stained pathological images were scanned to WSIs by a whole-slide scanner KF-PRO-005-HI (Konfoong Biotech International Co., Ltd.) which has a high-resolution(Figure 1). Based on morphological heterogeneity information of adenoid cystic carcinoma and basal cell adenoma. We use popular convolutional neural networks (Efficietnet-B5, resnet50 and transformer) to establish a deep learning model, carry out weakly supervised learning and supervised learning respectively, and then the random forest was introduced to feature extractions and slide-based classification

Results: In the present study, we propose a deep learning-based framework to classify morphological changes occurring in ACC or ABC. The overall performance of our model in slide-based differentiation of adenoid cystic carcinoma was very excellent. The highest AUC score was 0.91 in the supervised learning task and 0.85 in the weakly supervised learning task(Figure 2).
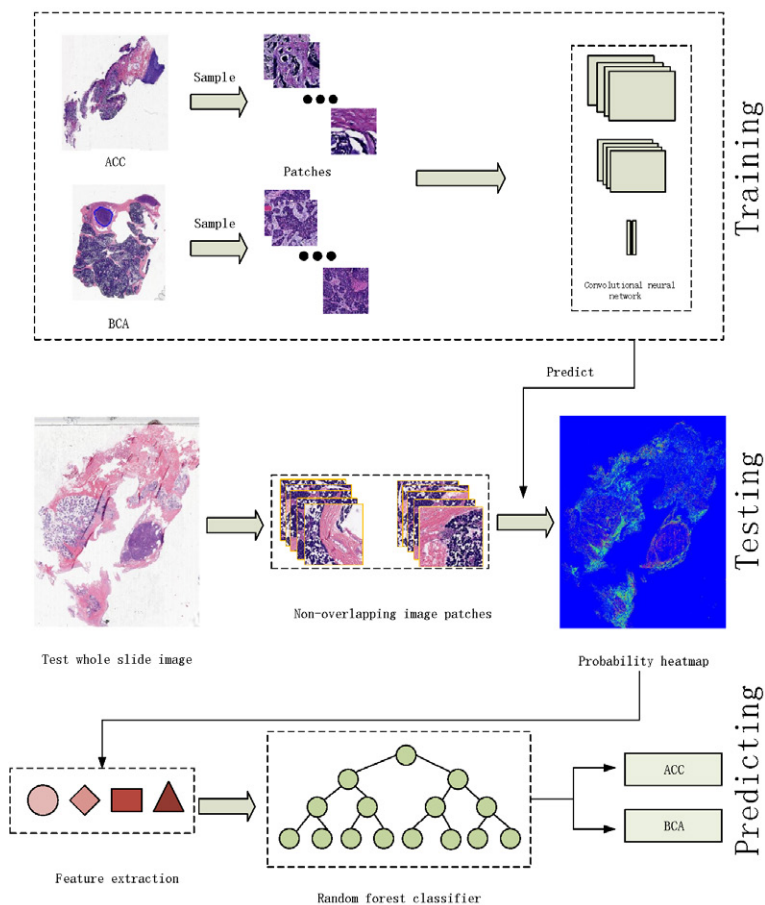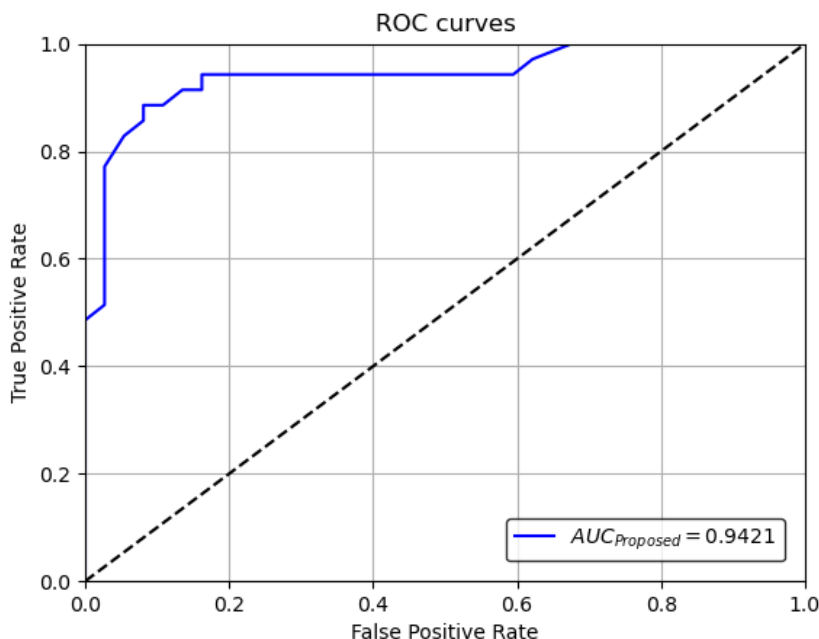
Figure 1 - 1170

Figure 2 - 1170

Conclusions: The application of advanced artificial intelligence (AI) techniques coupled with Pathological imaging can be helpful for the accurate detection of diseases. We successfully designed a novel deep learning model to assist in the diagnosis of salivary gland tumors accurately. As far as we have known, our analysis is the first computer-aided diagnosis based on pathological images of adenoid cystic carcinoma and basal cell adenoma. Research shows that this method can assist pathologists in clinical diagnosis and accelerate the diagnosis process.

1171 A Liquid Biopsy-Based HCC Extracellular Vesicle Digital Scoring Assay for Early Detection of HCC

Yazhen Zhu[1], Na Sun[2], Ceng Zhang[3], Yi-Te Lee[2], Ju Dong Yang[4], Vatche Agopian[3], Hsian-Rong Tseng[2]
[1]University of California, Los Angeles, Los Angeles, CA, [2]David Geffen School of Medicine at UCLA, Los Angeles, CA, [3]UCLA Medical Center and David Geffen School of Medicine, Los Angeles, CA, [4]Cedars-Sinai Medical Center, Los Angeles, CA

Disclosures: Yazhen Zhu: None; Na Sun: None; Ceng Zhang: None; Yi-Te Lee: None; Ju Dong Yang: None; Vatche Agopian: None; Hsian-Rong Tseng: *Stock Ownership*, CytoLumina Technologies Corp

Background: It is critical to detect Hepatocellular carcinoma (HCC) earlier when the curative-intent treatments are available to reduce the high HCC mortality rates. Therefore, a non-invasive diagnostic solution for early detection of HCC is desperately needed. Extracellular Vesicles (EVs) are phospholipid bilayer-enclosed particles that are released by all types of cells, and even more so by tumor cells. This study aimed to develop and validate an EV-based digital scoring assay that combines the isolation of HCC-derived EVs and digital PCR for detecting early-stage HCC from at-risk chronic liver disease.

Design: Plasma samples of 113 patients from early-stage HCC (n = 62, Barcelona Clinic Liver Cancer (BCLC) stage 0-A) and at-risk chronic liver disease control cohort (n = 51) were recruited in this study. HCC EV digital scoring assay that combines isolation of HCC EVs from plasma samples and Reverse-transcriptase digital PCR (RT-dPCR) was developed and validated. Stepwise logistic regression analysis was conducted based on the copy numbers of the 8 HCC EV genes and leave-one-out cross-validation (LOOCV) was performed to validate the selected logistic regression model for differentiating early-stage HCC versus controls. The area under the receiver operating characteristic curve (AUC) was used to evaluate the diagnostic accuracy.

Results: As depicted in the heat maps and boxplot, Higher signals are observed in early-stage HCC patients compared with the control group (patients with at-risk chronic liver diseases) (Fig. 1A, and B). The AUC for the HCC EV digital score for differentiating

HCC versus Controls is 0.87 (95% CI, 0.80 to 0.93; sensitivity = 80.0%, specificity = 88.2%) and 0.86 (95% CI, 0.78 to 0.92; sensitivity = 77.4%, specificity = 84.3%) before and after LOOCV, respectively (Fig. 1C, and D). The ROC curves showed a slight change in model performance with and without cross-validation. Moreover, ROC curves showed that the AUC for the HCC EV digital score for differentiating early-stage HCC (BCLC stage 0-A) versus at-risk chronic liver diseases outperformed the AUC for serum AFP test (0.87 versus 0.72, p < 0.05).

Figure 1 - 1171
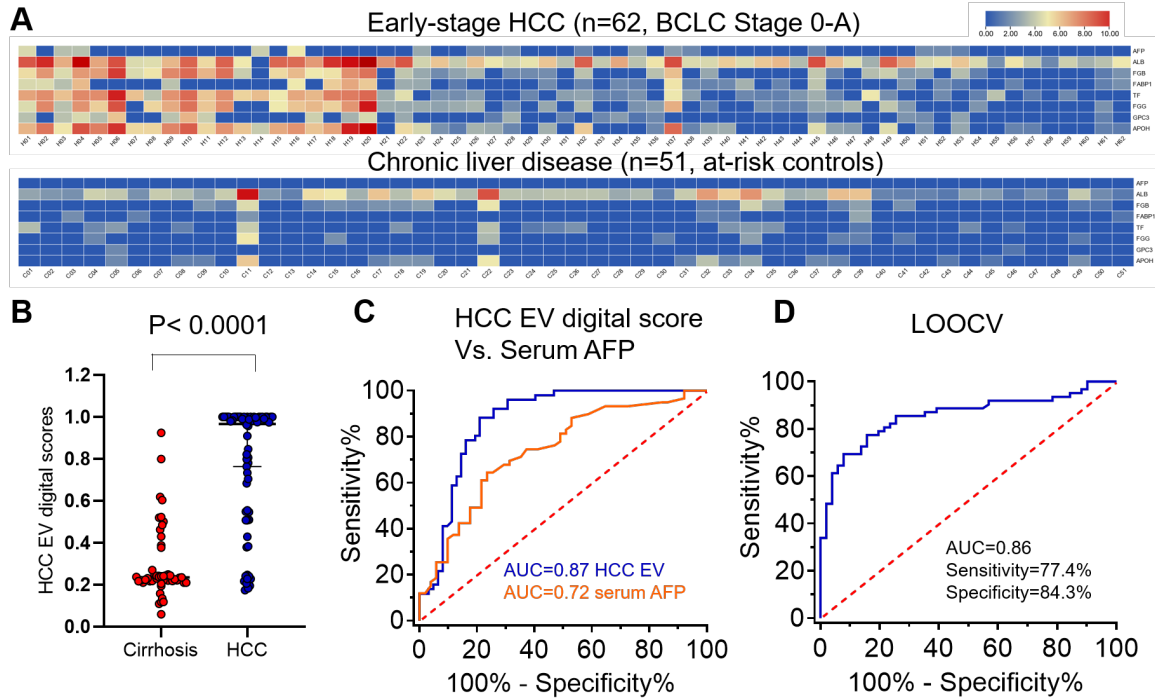
Conclusions: We developed and validated an HCC EV digital scoring assay that combines the isolation of HCC EVs and quantification of HCC EV-associated genes in the isolated HCC EVs for early detection of HCC. This liquid biopsy-based noninvasive assay holds great potential to augment the ability of current diagnosis criteria to realize early detection of HCC.